CHAPTER FIVE

# Bandpass Radome

**ROBERT G. SCHMIER,** Westinghouse Electric Corporation, Electronic Systems Group, Baltimore, Maryland

Bandpass radomes are most often constructed from one or more metallic screens sandwiched between dielectric slabs. The metallic screens are perforated in a regular pattern such that at the design resonant frequency the radome passes nearly 100% of the energy incident on it. Outside the design passband, nearly all the incident energy is reflected. In essence, these radomes provide a bandpass filter function to the antennas located behind them.

The metallic screens used in these radomes can be essentially infinitesimally thin or electrically thick. In this chapter, both thick-screen and thin-screen bandpass radomes are described. In addition, the analysis required to design these radomes is presented along with the performance of several prototype bandpass radomes.

## 5.1 THICK-SCREEN FSS

Thick-screen bandpass radomes contain elements in a regular grid pattern that are formed in an electrically thick conductive plate. In the analysis of these thick-screen frequency selective surfaces (FSS), one cannot assume that element thickness has little influence on the radome's behavior, as is the case with thin-screen FSSs. In this section, one method of analyzing a general thick-screen FSS will be shown where an equivalent problem is established that allows separating the larger problem into more easily solved parts. This

*Frequency Selective Surface and Grid Array*, Edited by T. K. Wu
ISBN 0-471-31189-8 © 1995 John Wiley & Sons, Inc.

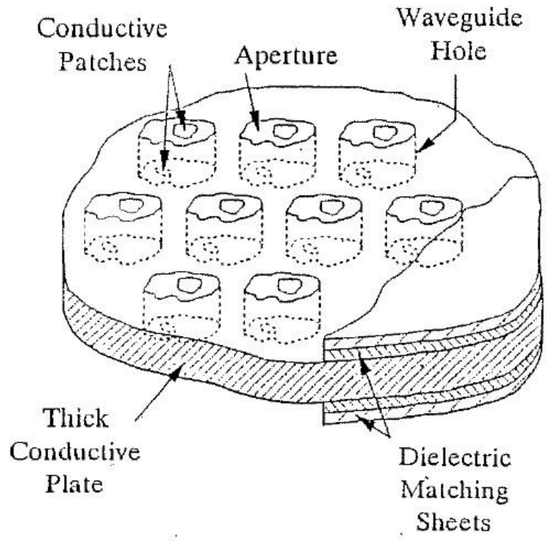


FIGURE 5.1 General thick-screen bandpass radome geometry.

analysis technique is then used to solve for the transmission and reflection properties of several specific thick-screen FSS geometries.

### 5.1.1 Thick-Screen FSS Geometry

Figure 5.1 shows the general geometry of a single-thick-screen FSS that is analyzed here. The FSS is assumed to extend infinitely in the $x$-$y$ plane with the grid defined in Figure 5.2. Every element in the FSS is assumed to be an identical arbitrary cross-sectional waveguide element and to have an arbitrary, but fixed, shape in any cut through a plane parallel to the $x$-$y$ plane. In other words, the shape of the element is fixed along the $z$ axis. Any number of dielectrics is allowed on either side of the conductive thick screen and inside the element formed in the screen. Conductive patches that form irises are also allowed at the apertures on either side of the thick screen.

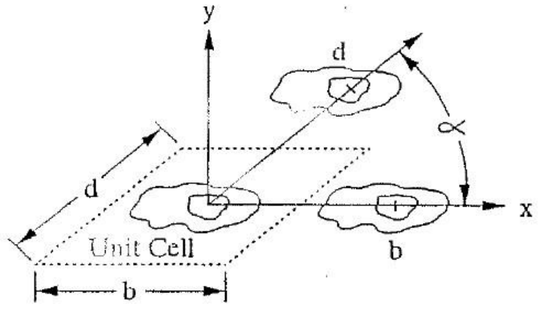


FIGURE 5.2 Grid definition showing a unit cell of the bandpass radome.



### 5.1.2 Equivalent Problem Formulation

The first step in analyzing the thick-screen FSS is to establish an equivalent problem. In the equivalent problem for a single element of the thick-screen FSS (see Figure 5.3), the apertures formed on either side of the thick screen are replaced by perfect conductors, and sheets of magnetic current are placed on top of the conductor on both sides of the aperture [1, 2]. Placement of these magnetic currents ensures continuity of the tangential electric field across the aperture in the equivalent problem. Magnetic currents on opposite sides of the aperture are of equal magnitude and opposite sign.

An equivalent problem established in this manner is identical to the original problem, but the analysis in the equivalent problem can be conveniently separated into three distinct regions (Figure 5.3): region A to the left side of the thick screen, region B a waveguide region in the screen itself, and region C to the right side of the thick screen. These regions can be analyzed separately and are coupled together by the magnetic currents at the apertures.

### 5.1.3 General Problem Solution

After establishing an equivalent problem for determining the transmission and reflection properties of the thick-screen FSS, we can obtain a solution by employing a spectral moment method solution to the magnetic-field integral equation. This solution will rigorously take into account various dielectric layers and thick-screen waveguide fillers for the general case of an element with arbitrary cross section as shown in Figure 5.1.

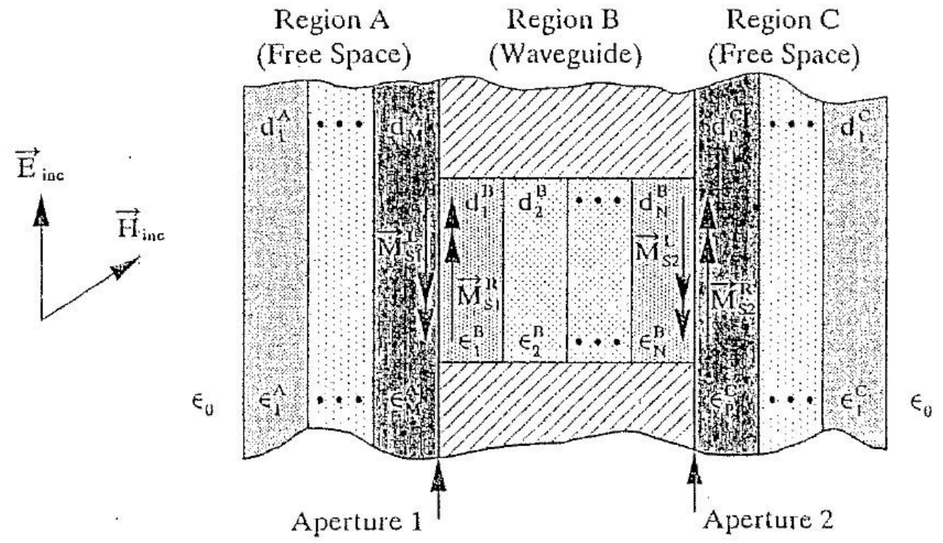


FIGURE 5.3 Equivalent problem for analyzing a thick-screen bandpass radome including stratified dielectric layers.

To solve this problem, we must determine the fields from the infinite array of thick-screen elements. If one assumes that the magnetic currents of every element of the FSS have identical shape and equal magnitude, but have a linear phase shift based on the angle of incidence of an impinging plane wave, then Floquet's theorem can be employed and the field from the infinite array can be expanded in an infinite number of plane waves [3, 4]. Hence, a spectral moment method solution is appropriate for this problem since it will express the fields radiated by the infinite array of magnetic currents as an infinite sum or spectrum of plane waves.

Since the fields at every element are identical, with the exception of a phase shift, only a single unit cell of the FSS as shown in Figure 5.2 needs to be considered in the analysis to determine the properties of the overall thick-screen FSS. To solve for the fields within this unit cell, one needs to enforce continuity of the tangential electric and magnetic fields across the apertures of the thick-screen FSS. At aperture 1, as defined in Figure 5.3,

$$\mathbf{E}_T^{1L} = \mathbf{E}_T^{1R}, \quad \mathbf{H}_T^{1L} = \mathbf{H}_T^{1R}, \tag{5.1}$$

where $\mathbf{E}_T^{1L}$ and $\mathbf{H}_T^{1L}$ represent the tangential electric and magnetic fields to the left side of aperture 1 and $\mathbf{E}_T^{1R}$ and $\mathbf{H}_T^{1R}$ represent the tangential electric and magnetic fields to the right side of aperture 1. Similarly, at aperture 2,

$$\mathbf{E}_T^{2L} = \mathbf{E}_T^{2R}, \quad \mathbf{H}_T^{2L} = \mathbf{H}_T^{2R}. \tag{5.2}$$

The remainder of the analysis is based on the simple relations set forth in (5.1) and (5.2), which enforce continuity of tangential electric and magnetic fields across the thick-screen FSS apertures.

*Expansion of the Tangential Aperture Fields into Modes* The tangential electric and magnetic fields in all three regions and at the apertures of this problem, as shown in Figure 5.3, can be expressed as infinite sums of electromagnetic modes. This is exactly analogous to expressing an arbitrary waveform as an infinite sum of sine and cosine functions in a Fourier series. To represent the tangential fields accurately in all regions of this problem, we should choose carefully the basic functions that will be expanded over.

The natural choice of basis functions to the left and right sides of the thick screen, regions A and C respectively, is Floquet or free-space-mode functions, which are plane waves based on the FSS grid. The fields inside the thick screen can be expressed as an infinite sum of waveguide-mode functions that are natural for the cross section of the thick-screen element. At the apertures the magnetic currents are also expressed as an infinite sum of modes whose chosen form depends on the geometry of the aperture. The Floquet and waveguide modes are full-domain basis functions that cover the entire unit cell of the element. The problem converges much faster if the magnetic current modes at the apertures are also chosen to be full-domain



basis functions, as opposed to pulse or some similar type function; that is, if the aperture is coaxial, then a natural set of basis functions to choose in the aperture may be coaxial waveguide functions.

All of the chosen basis functions are completely defined by the geometry, frequency, and incidence angle of the plane wave exciting the FSS. They are also chosen here such that the basis functions representing the magnetic field are orthonormal. For example, if $\mathbf{h}_m^F$ and $\mathbf{h}_i^F$ represent the tangential components of the magnetic field of two Floquet-mode basis functions, then

$$\langle \mathbf{h}_m^F, \mathbf{h}_i^F \rangle = \iint_{\substack{\text{unit} \\ \text{cell}}} \mathbf{h}_m^F \cdot \mathbf{h}_i^{F*}\, dA = \delta_{mi},$$

where the integration extends over the unit cell and $\delta_{mi}$ represents the Dirac delta function, which is unity when $m = i$ and is zero otherwise.

Referring to Figure 5.3, the field scattered by the magnetic current on the left side of aperture 1, $\mathbf{M}_{S1}^L$, can now be determined for the case where no dielectrics are present. The magnetic current $\mathbf{M}_{S1}^L$ scatters a field to the left, $\mathbf{E}^L$, and to the right, $\mathbf{E}^R$, as shown in Figure 5.4. The field scattered to the left, $\mathbf{E}^L$, can be expressed in terms of Floquet-mode electric-field basis functions as follows:

$$\mathbf{E}^L = \sum_m A_m \mathbf{e}_m^F,$$

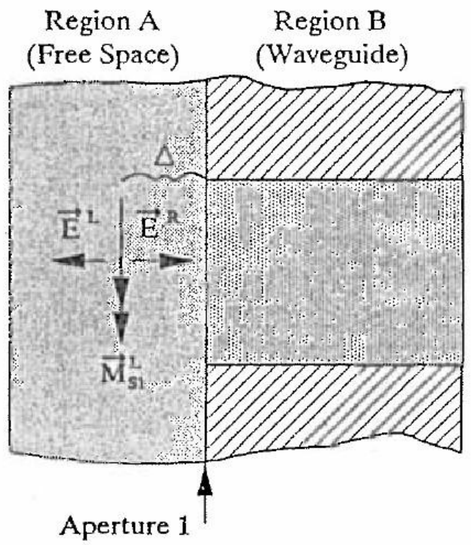


**FIGURE 5.4** Electric field scattered by $\mathbf{M}_{S1}^L$ on the left side of aperture 1.

where $A_m$ represent unknown coefficients and $\mathbf{e}_m^F$ are related to the magnetic-field Floquet-mode basis functions as follows:

$$\mathbf{e}_m^F = \frac{1}{Y_m}\mathbf{h}_m^F \times \hat{z}$$

and

$$\langle \mathbf{e}_m, \mathbf{e}_i \rangle = \frac{1}{|Y_m|^2}\delta_{mi},$$

where $Y_m$ is the admittance of the media just to the left of the thick screen for the Floquet mode of index $m$. The field scattered to the right is, similarly,

$$\mathbf{E}^R = -\sum_m A_m \mathbf{e}_m^F.$$

The magnetic current $\mathbf{M}_{S1}^L$ is related to $\mathbf{E}^L$ and $\mathbf{E}^R$ as follows:

$$(\mathbf{E}^L - \mathbf{E}^R) \times -\hat{z} = \mathbf{M}_{S1}^L.$$

Substituting for $\mathbf{E}^L$ and $\mathbf{E}^R$, we obtain

$$2\sum_m A_m \mathbf{e}_m^F \times -\hat{z} = \mathbf{M}_{S1}^L, \qquad 2\sum_m A_m \mathbf{e}_m^F = -\hat{z} \times \mathbf{M}_{S1}^L, \tag{5.3}$$

which is the total field scattered to the left by $\mathbf{M}_{S1}^L$.

Now one can take advantage of the orthonormality of the Floquet-mode functions by applying it to (5.3) as follows:

$$\left\langle 2\sum_m A_m \mathbf{e}_m^F, \mathbf{e}_i^F \right\rangle = \langle -\hat{z} \times \mathbf{M}_{S1}^L, \mathbf{e}_i^F \rangle,$$

$$2\iint_{\text{unit cell}} \sum_m A_m \mathbf{e}_m^F \cdot \mathbf{e}_i^{F*}\, dA = \iint_{\text{unit cell}} -\hat{z} \times \mathbf{M}_{S1}^L \cdot \mathbf{e}_i^{F*}\, dA,$$

$$2A_i \frac{1}{|Y_i|^2} = \langle -\hat{z} \times \mathbf{M}_{S1}^L, \mathbf{e}_i \rangle,$$

$$A_i = \tfrac{1}{2}\langle -\hat{z} \times \mathbf{M}_{S1}^L, \mathbf{e}_i \rangle |Y_i|^2. \tag{5.4}$$

The corresponding total magnetic field scattered to the left by $\mathbf{M}_{S1}^L$ is

$$\mathbf{H}_{MS1}^{1L} = -2\sum_m A_m \mathbf{h}_m^F. \tag{5.5}$$



Substituting (5.4) into (5.5) yields

$$\mathbf{H}_{MS1}^{1L} = -2\sum_m \langle Y_m \mathbf{M}_{S1}^L, \mathbf{h}_m^F \rangle \mathbf{h}_m^F. \tag{5.6}$$

Equation 5.6 represents the total tangential magnetic field scattered to the left of the thick-screen FSS by $\mathbf{M}_{S1}^L$ as an infinite sum of Floquet modes. The effect of stratified dielectrics to the left of the thick screen can be included in (5.6) by the simple introduction of an additional term as follows:

$$\mathbf{H}_{MS1}^{1L} = -\sum_m Y_m^{MA} \frac{T_{1,1}^L}{2} \langle \mathbf{M}_{S1}^L, \mathbf{h}_m^F \rangle \mathbf{h}_m^F, \tag{5.7}$$

where $Y_m^{MA}$ is the admittance of the dielectric layer in which $\mathbf{M}_{S1}^L$ resides for a Floquet mode of index $m$, and $T_{1,1}^L$ includes stratified dielectric effects and is referred to here as a $T$-factor. It is determined by the dielectric slab geometry and will be defined later.

In the absence of any external dielectric sheets on the left side of the screen, the magnetic field at the aperture at the left side of the FSS due to the incident field is

$$\mathbf{H}_{\text{inc}}^{1L} = 2\mathbf{H}_{\text{inc}},$$

where $\mathbf{H}_{\text{inc}}$ is the incident magnetic field and the factor of 2 is due to the reflection of the magnetic field off the perfect conductor. To include the effect of stratified dielectrics, we include a $T$-factor to yield

$$\mathbf{H}_{\text{inc}}^{1L} = T_{\text{inc}} \mathbf{H}_{\text{inc}}. \tag{5.8}$$

The sum of (5.7) and (5.8) yields the total tangential magnetic field on the left side of aperture 1, $\mathbf{H}_T^{1L}$, as follows:

$$\mathbf{H}_T^{1L} = \mathbf{H}_{\text{inc}}^{1L} + \mathbf{H}_{MS1}^{1L}$$

$$= T_{\text{inc}}\mathbf{H}_{\text{inc}} - \sum_m Y_m^{MA} \frac{T_{1,1}^L}{2} \langle \mathbf{M}_{S1}^L, \mathbf{h}_m^F \rangle \mathbf{h}_m^F. \tag{5.9}$$

The first component represents the field due to the incident field. The second component represents the fields scattered by the magnetic current on the left side of aperture 1, $\mathbf{M}_{S1}^L$.

The fields on the right side of aperture 1 are generated similarly. The magnetic field at the right side of aperture 1 due to the current at the right

side of aperture 1, $\mathbf{M}_{S1}^{R}$, is

$$\mathbf{H}_{MS1}^{1R} = -\sum_n Y_n^{1B} \frac{T_{1,1}^{R}}{2} \langle \mathbf{M}_{S1}^{R}, \mathbf{h}_n^{WG} \rangle \mathbf{h}_n^{WG}, \tag{5.10}$$

where $\mathbf{h}_n^{WG}$ represents orthonormal magnetic-field waveguide-mode functions within the thick screen, $Y_n^{1B}$ represents the admittance of the dielectric just to the right of aperture 1 for a waveguide mode of index $n$, and $T_{1,1}^{R}$ (to be defined later) is another $T$-factor that includes dielectric effects. The magnetic field at the right side of aperture 1 due to the magnetic current at the left side of aperture 2, $\mathbf{M}_{S2}^{L}$, is

$$\mathbf{H}_{MS2}^{1R} = -\sum_n Y_n^{NB} \frac{T_{1,2}}{2} \langle \mathbf{M}_{S2}^{L}, \mathbf{h}_n^{WG} \rangle \mathbf{h}_n^{WG}, \tag{5.11}$$

where again $\mathbf{h}_n^{WG}$ represent magnetic-field waveguide-mode functions, $Y_n^{NB}$ is the admittance of the dielectric layer $N$ just to the left of aperture 2 for waveguide mode $n$, and $T_{1,2}$ (to be defined later) is the $T$-factor that relates the fields at aperture 1 to the fields at aperture 2. The total field to the right side of aperture 1 is the sum of (5.10) and (5.11):

$$\begin{aligned} \mathbf{H}_T^{1R} &= \mathbf{H}_{MS1}^{1R} + \mathbf{H}_{MS2}^{1R} \\ &= -\sum_n Y_n^{1B} \frac{T_{1,1}^{R}}{2} \langle \mathbf{M}_{S1}^{R}, \mathbf{h}_n^{WG} \rangle \mathbf{h}_n^{WG} - \sum_n Y_n^{NB} \frac{T_{1,2}}{2} \langle \mathbf{M}_{S2}^{L}, \mathbf{h}_n^{WG} \rangle \mathbf{h}_n^{WG}, \end{aligned} \tag{5.12}$$

where it is convenient, but not necessary, for the summation indices to be identical.

Following a similar procedure, we obtain the tangential magnetic fields on the left side of aperture 2:

$$\mathbf{H}_T^{2L} = -\sum_n Y_n^{NB} \frac{T_{2,2}^{L}}{2} \langle \mathbf{M}_{S2}^{L}, \mathbf{h}_n^{WG} \rangle \mathbf{h}_n^{WG} - \sum_n Y_n^{1B} \frac{T_{2,1}}{2} \langle \mathbf{M}_{S1}^{R}, \mathbf{h}_n^{WG} \rangle \mathbf{h}_n^{WG}, \tag{5.13}$$

where the first term in (5.13) represents the tangential magnetic field at the left side of aperture 2 due to the magnetic current at the left side of aperture 2, and the second term is due to the field scattered by the magnetic current at the right side of aperture 1. Similarly, the tangential magnetic field on the



right side of aperture 2 is

$$\mathbf{H}_T^{2R} = -\sum_m Y_m^{PC} \frac{T_{2,2}^{R}}{2} \langle \mathbf{M}_{S2}^{R}, \mathbf{h}_m^{F} \rangle \mathbf{h}_m^{F}, \tag{5.14}$$

which is simply the field scattered by the magnetic current on the right side of aperture 2.

By combining (5.1) and (5.2), which equate tangential magnetic fields across the aperture, with (5.9), (5.12), (5.13), and (5.14), we find the following set of general equations that define this problem:

$$\begin{aligned} T_{\text{inc}}\mathbf{H}_{\text{inc}} &= \sum_m Y_m^{MA} \frac{T_{1,1}^{L}}{2} \langle \mathbf{M}_{S1}^{L}, \mathbf{h}_m^{F} \rangle \mathbf{h}_m^{F} - \sum_n Y_n^{1B} \frac{T_{1,1}^{R}}{2} \langle \mathbf{M}_{S1}^{R}, \mathbf{h}_n^{WG} \rangle \mathbf{h}_n^{WG} \\ &\quad - \sum_n Y_n^{NB} \frac{T_{1,2}}{2} \langle \mathbf{M}_{S2}^{L}, \mathbf{h}_n^{WG} \rangle \mathbf{h}_n^{WG}, \\ 0 &= \sum_m Y_m^{PC} \frac{T_{2,2}^{R}}{2} \langle \mathbf{M}_{S2}^{R}, \mathbf{h}_m^{F} \rangle \mathbf{h}_m^{F} - \sum_n Y_n^{1B} \frac{T_{2,1}}{2} \langle \mathbf{M}_{S1}^{R}, \mathbf{h}_n^{WG} \rangle \mathbf{h}_n^{WG} \\ &\quad - \sum_n Y_n^{NB} \frac{T_{2,2}^{L}}{2} \langle \mathbf{M}_{S2}^{L}, \mathbf{h}_n^{WG} \rangle \mathbf{h}_n^{WG}. \end{aligned} \tag{5.15}$$

The magnetic current modes $\mathbf{M}_{S1}^{L}$, $\mathbf{M}_{S1}^{R}$, $\mathbf{M}_{S2}^{L}$, and $\mathbf{M}_{S2}^{R}$ can now be expanded into orthonormal modes as follows:

$$\mathbf{M}_{S1}^{L} = \sum_p A_p \mathbf{e}_p^1 = -\mathbf{M}_{S1}^{R}, \qquad \mathbf{M}_{S2}^{L} = \sum_q B_q \mathbf{e}_q^2 = -\mathbf{M}_{S2}^{R}$$

where $A_p$ and $B_q$ are the unknown coefficients to be determined, $\mathbf{e}_p^1$ are orthonormal magnetic current modes at aperture 1, and $\mathbf{e}_q^2$ are orthonormal magnetic current modes at aperture 2. Note that neither $\mathbf{e}_p^1$ nor $\mathbf{e}_q^2$ are required to be orthonormal or even orthogonal over their domains, but for convenience they have been chosen to be so here (for example, overlapping piecewise sinusoidal functions are not orthogonal, but are often used in moment method analysis). Also note that, in general, $\mathbf{e}_p^1$ and $\mathbf{e}_q^2$ are not the

same and are necessarily different when aperture 1 is not identical to aperture 2. These magnetic currents are substituted back into (5.15) to yield

$$\begin{aligned}
T_{\text{inc}}\mathbf{H}_{\text{inc}} = {} & \sum_m Y_m^{MA}\frac{T_{1,1}^L}{2}\left\langle\sum_p A_p\mathbf{e}_p^1, \mathbf{h}_m^F\right\rangle\mathbf{h}_m^F \\
& + \sum_n Y_n^{1B}\frac{T_{1,1}^R}{2}\left\langle\sum_p A_p\mathbf{e}_p^1, \mathbf{h}_n^{WG}\right\rangle\mathbf{h}_n^{WG} \\
& - \sum_n Y_n^{NB}\frac{T_{1,2}}{2}\left\langle\sum_q B_q\mathbf{e}_q^2, \mathbf{h}_n^{WG}\right\rangle\mathbf{h}_n^{WG}, \\
0 = {} & -\sum_m Y_m^{PC}\frac{T_{2,2}^R}{2}\left\langle\sum_q B_q\mathbf{e}_q^2, \mathbf{h}_m^F\right\rangle\mathbf{h}_m^F \\
& + \sum_n Y_n^{1B}\frac{T_{2,1}}{2}\left\langle\sum_p A_p\mathbf{e}_p^1, \mathbf{h}_n^{WG}\right\rangle\mathbf{h}_n^{WG} \\
& - \sum_n Y_n^{NB}\frac{T_{2,2}^L}{2}\left\langle\sum_q B_q\mathbf{e}_q^2, \mathbf{h}_n^{WG}\right\rangle\mathbf{h}_n^{WG}. \qquad (5.16)
\end{aligned}$$

If one now tests or takes the inner product of each side of the first equation in (5.16) with $\mathbf{e}_i^1$ and each side of the second equation in (5.16) with $\mathbf{e}_j^2$ the following equations result:

$$\begin{aligned}
T_{\text{inc}}\langle\mathbf{e}_i^1, \mathbf{H}_{\text{inc}}\rangle^* = {} & \sum_p A_p\sum_m Y_m^{MA}\frac{T_{1,1}^L}{2}\langle\mathbf{e}_p^1, \mathbf{h}_m^F\rangle\langle\mathbf{e}_i^1, \mathbf{h}_m^F\rangle^* \\
& + \sum_p A_p\sum_n Y_n^{1B}\frac{T_{1,1}^R}{2}\langle\mathbf{e}_p^1, \mathbf{h}_n^{WG}\rangle\langle\mathbf{e}_i^1, \mathbf{h}_n^{WG}\rangle \\
& - \sum_q B_q\sum_n Y_n^{NB}\frac{T_{1,2}}{2}\langle\mathbf{e}_q^2, \mathbf{h}_n^{WG}\rangle\langle\mathbf{e}_i^1, \mathbf{h}_n^{WG}\rangle, \\
0 = {} & \sum_p A_p\sum_n Y_n^{1B}\frac{T_{2,1}}{2}\langle\mathbf{e}_p^1, \mathbf{h}_n^{WG}\rangle\langle\mathbf{e}_j^2, \mathbf{h}_n^{WG}\rangle \\
& - \sum_q B_q\sum_m Y_m^{PC}\frac{T_{2,2}^R}{2}\langle\mathbf{e}_q^2, \mathbf{h}_m^F\rangle\langle\mathbf{e}_j^2, \mathbf{h}_m^F\rangle^* \\
& - \sum_q B_q\sum_n Y_n^{NB}\frac{T_{2,2}^L}{2}\langle\mathbf{e}_q^2, \mathbf{h}_n^{WG}\rangle\langle\mathbf{e}_j^2, \mathbf{h}_n^{WG}\rangle, \qquad (5.17)
\end{aligned}$$

where the $\mathbf{h}_n^{WG}$ are orthonormal waveguide modes, $\mathbf{h}_m^F$ are orthonormal Floquet modes, and $\mathbf{e}_p^1$ and $\mathbf{e}_q^2$ are chosen to be orthonormal magnetic



current modes. In (5.17), the index $i$ runs from 1 to $p$ to yield $p$ equations, and the index $j$ runs from 1 to $q$ to yield $q$ equations. The combination yields $p + q$ equations in $p + q$ unknowns. The equations can be put in an admittance matrix form to solve for the unknowns $A_p$ and $B_q$:

$$\left[\begin{array}{c} I_1^{\text{inc}} \\ I_2^{\text{inc}} \\ \vdots \\ I_p^{\text{inc}} \\ \hline 0 \\ 0 \\ \vdots \\ 0 \end{array}\right] = \left[\begin{array}{cccc|cccc} Y_{1,1}^{1,1} & Y_{1,2}^{1,1} & \cdots & Y_{1,P}^{1,1} & Y_{1,1}^{1,2} & Y_{1,2}^{1,2} & \cdots & Y_{1,Q}^{1,2} \\ Y_{2,1}^{1,1} & Y_{2,2}^{1,1} & \cdots & Y_{2,P}^{1,1} & Y_{2,1}^{1,2} & Y_{2,2}^{1,2} & \cdots & Y_{2,Q}^{1,2} \\ \vdots & \vdots & & \vdots & \vdots & \vdots & & \vdots \\ Y_{P,1}^{1,1} & Y_{P,2}^{1,1} & \cdots & Y_{P,P}^{1,1} & Y_{P,1}^{1,2} & Y_{P,2}^{1,2} & \cdots & Y_{P,Q}^{1,2} \\ \hline Y_{1,1}^{2,1} & Y_{1,2}^{2,1} & \cdots & Y_{1,P}^{2,1} & Y_{1,1}^{2,2} & Y_{1,2}^{2,2} & \cdots & Y_{1,Q}^{2,2} \\ Y_{2,1}^{2,1} & Y_{2,2}^{2,1} & \cdots & Y_{2,P}^{2,1} & Y_{2,1}^{2,2} & Y_{2,2}^{2,2} & \cdots & Y_{2,Q}^{2,2} \\ \vdots & \vdots & & \vdots & \vdots & \vdots & & \vdots \\ Y_{Q,1}^{2,1} & Y_{Q,2}^{2,1} & \cdots & Y_{Q,P}^{2,1} & Y_{Q,1}^{2,2} & Y_{Q,2}^{2,2} & \cdots & Y_{Q,Q}^{2,2} \end{array}\right] \times \left[\begin{array}{c} A_1 \\ A_2 \\ \vdots \\ A_p \\ \hline B_1 \\ B_2 \\ \vdots \\ B_Q \end{array}\right], \qquad (5.18)$$

where

$$\begin{aligned}
I_i^{\text{inc}} &= 2T_{\text{inc}}\langle\mathbf{e}_i^1, \mathbf{H}_{\text{inc}}\rangle^*, \\
Y_{i,j}^{1,1} &= \sum_m Y_m^{MA}T_{1,1}^L\langle\mathbf{e}_j^1, \mathbf{h}_m^F\rangle\langle\mathbf{e}_i^1, \mathbf{h}_m^F\rangle^* + \sum_n Y_n^{1B}T_{1,1}^R\langle\mathbf{e}_j^1, \mathbf{h}_n^{WG}\rangle\langle\mathbf{e}_i^1, \mathbf{h}_n^{WG}\rangle, \\
Y_{i,j}^{1,2} &= -\sum_n Y_n^{NB}T_{1,2}\langle\mathbf{e}_j^2, \mathbf{h}_n^{WG}\rangle\langle\mathbf{e}_i^1, \mathbf{h}_n^{WG}\rangle, \\
Y_{i,j}^{2,1} &= \sum_n Y_n^{1B}T_{2,1}\langle\mathbf{e}_j^1, \mathbf{h}_n^{WG}\rangle\langle\mathbf{e}_i^2, \mathbf{h}_n^{WG}\rangle, \\
Y_{i,j}^{2,2} &= -\sum_m Y_m^{PC}T_{2,2}^R\langle\mathbf{e}_j^2, \mathbf{h}_m^F\rangle\langle\mathbf{e}_i^2, \mathbf{h}_m^F\rangle^* - \sum_n Y_n^{NB}T_{2,2}^L\langle\mathbf{e}_j^2, \mathbf{h}_n^{WG}\rangle\langle\mathbf{e}_i^2, \mathbf{h}_n^{WG}\rangle.
\end{aligned}$$

This system of equations is solved for the unknowns $A_i$ and $B_i$, where $A_i$ represent the coefficients of the magnetic current modes on the left side of

aperture 1, and $B_i$ represent the magnetic current modes on the left side of aperture 2. They are used in conjunction with (5.9) and (5.14) to yield the total reflected and transmitted magnetic fields for the thick-screen FSS.

***T*-Factor Definition** The $T$-factor is used here to relate the magnetic field at one aperture to the magnetic field scattered by a current mode at the same aperture, or at another aperture, and to include the effects of stratified dielectrics. Figure 5.5 shows the geometry inside the waveguide of the thick-screen FSS for determining the $T$-factor $T_{2,1}$ that relates the magnetic field at aperture 2 due to the magnetic field scattered by the currents at aperture 1. Note that the form of $T_{2,1}$ is identical for every waveguide mode, but the actual values differ because every mode has its own propagation constant and impedance associated with it.

Figure 5.6 shows how the magnetic current at aperture 1 scatters energy to the magnetic current at aperture 2. Figure 5.6(a) shows the field scattered to the right by $\mathbf{M}_{S1}^{R}$, and Figure 5.6(b) shows the field scattered to the left by $\mathbf{M}_{S1}^{R}$. The total field scattered by $\mathbf{M}_{S1}^{R}$ is the sum of these two scattered fields. The multiple bounces created by the dielectric stratification must be accounted for. The contributions shown in Figure 5.6(a) from aperture 1 to aperture 2 are

$$\begin{aligned} T_{21} &= \tau_{1,N}^{e,B} + \tau_{1,N}^{e,B} + \left(\Gamma_{1,2}^{e,B} e^{-j2\gamma_1^B d_1^B}\right) 2\tau_{1,N}^{e,B} + \left(\Gamma_{1,2}^{e,B} e^{-j2\gamma_1^B d_1^B}\right)^2 2\tau_{1,N}^{e,B} \\ &\quad + \left(\Gamma_{1,2}^{e,B} e^{-j2\gamma_1^B d_1^B}\right)^3 2\tau_{1,N}^{e,B} + \cdots + \\ &= 2\tau_{1,N}^{e,B}\left(1 + \Gamma_{1,2}^{e,B} e^{-j2\gamma_1^B d_1^B} + \cdots\right), \end{aligned}$$

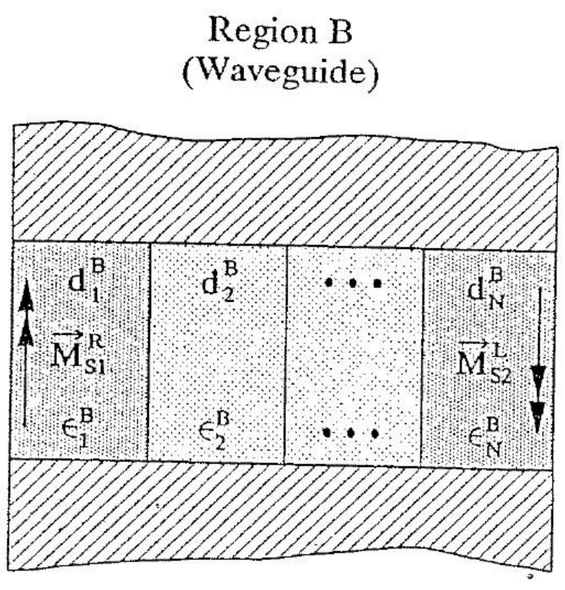


**FIGURE 5.5** Geometry inside the thick-screen FSS used to determine the $T$-factors $T_{2,1}$, $T_{1,2}$, $T_{1,1}^{R}$, and $T_{2,2}^{L}$.



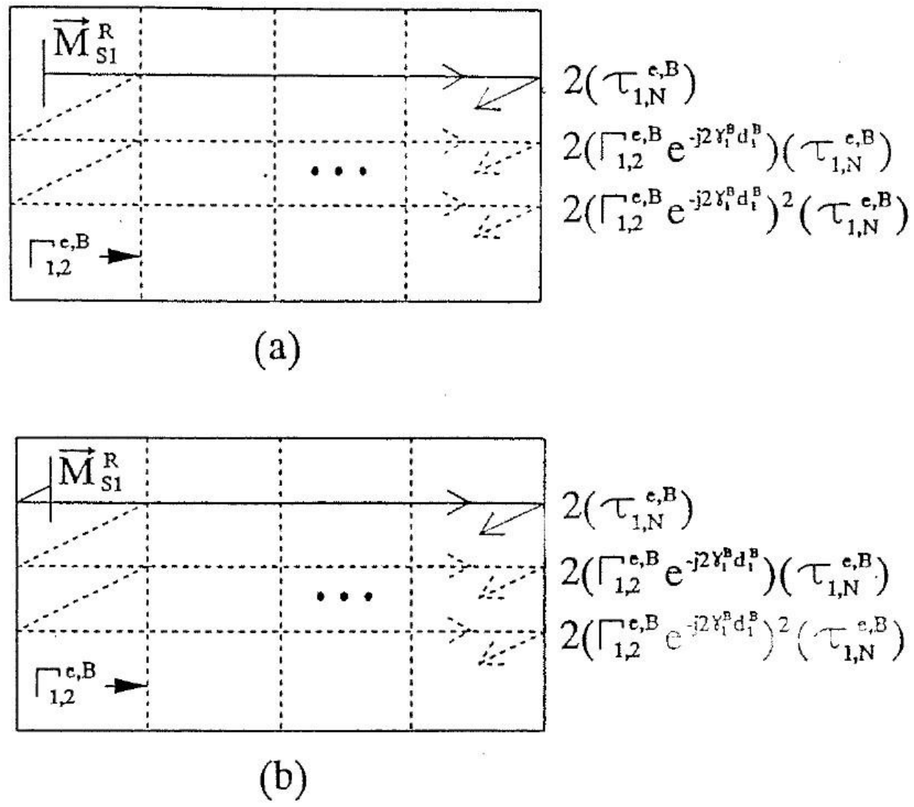


**FIGURE 5.6** Field at aperture 2 due to fields scattered by $\mathbf{M}_{S1}^{R}$: (a) field scattered to the right by $\mathbf{M}_{S1}^{R}$; (b) field scattered to the left by $\mathbf{M}_{S1}^{R}$.

which reduces to

$$2\tau_{1,N}^{e,B}/\left(1 - \Gamma_{1,2}^{e,B} e^{-j2\gamma_1^B d_1^B}\right),$$

where $\tau_{1,N}^{e,B}$ represents the effective transmission coefficient from aperture 1 to aperture 2, $\Gamma_{1,2}^{e,B}$ represents the effective reflection coefficient from dielectric layer 1 to dielectric layer 2, $\gamma_1^B$ represents the propagation constant in dielectric layer 1 for the waveguide mode of index $n$, and $d_1^B$ represents the thickness of dielectric layer 1. The superscript $B$ denotes that all terms refer to region $B$, or the waveguide region of the problem. The contributions from Figure 5.6(b) are, similarly,

$$T_{12} = 2\tau_{1,N}^{e,B}/\left(1 - \Gamma_{1,2}^{e,B} e^{-j2\gamma_1^B d_1^B}\right),$$

to yield a total $T$-factor relating the field at aperture 2 due to the field scattered by the magnetic current at aperture 1:

$$T_{2,1} = \frac{4\tau_{1,N}^{e,B}}{1 - \Gamma_{1,2}^{e,B} e^{-j2\gamma_1^B d_1^B}}. \tag{5.19}$$

In (5.19), the $\tau_{1,N}^{e,B}$ and $\Gamma_{1,2}^{e,B}$ terms are calculated in a recursive fashion. The generalized effective reflection coefficient looking from dielectric layer $m-1$ into dielectric layer $m$ is given in any region of the problem as

$$\Gamma_{m-1,m}^{e} = \frac{\Gamma_{m-1,m} + \Gamma_{m,m+1}^{e} e^{-j2\gamma_m d_m}}{1 + \Gamma_{m-1,m}\Gamma_{m,m+1}^{e} e^{-j2\gamma_m d_m}},$$

where $\Gamma_{m-1,m}$ is the Fresnel reflection coefficient between dielectric layers $m-1$ and $m$. To get $\Gamma_{1,2}^{e,B}$ in (5.19), one starts at aperture 2 and works back toward aperture 1, calculating effective reflection coefficients until $\Gamma_{1,2}^{e,B}$ is reached. In general, the effective transmission coefficient $\tau_{1,N}^{e}$ is calculated similarly as follows:

$$\tau_{1,N}^{e} = e^{-j\gamma_N d_N} \prod_{m=1}^{N-1} \tau_{m,m+1}^{e} e^{-j\gamma_m d_m},$$

where

$$\tau_{m,m+1}^{e} = \frac{\tau_{m,m+1}}{1 + \Gamma_{m,m+1}\Gamma_{m+1,m+2}^{e} e^{-j2\gamma_{m+1} d_{m+1}}}$$

and $\tau_{m,m+1}$ is the transmission coefficient between dielectric layers $m$ and $m+1$.

Following the same method, we find the remaining $T$-factors:

$$\begin{aligned}
T_{\text{inc}} &= 2\tau_{0,M}^{e,A}, \\
T_{1,1}^{L} &= \frac{2\left(1 + \Gamma_{M,M-1}^{e,A} e^{-j2\gamma_m^A d_m^A}\right)}{1 - \Gamma_{M,M-1}^{e,A} e^{-j2\gamma_m^A d_m^A}}, \\
T_{1,1}^{R} &= \frac{2\left(1 + \Gamma_{1,2}^{e,B} e^{-j2\gamma_1^B d_1^B}\right)}{1 - \Gamma_{1,2}^{e,B} e^{-j2\gamma_1^B d_1^B}}, \\
T_{1,2} &= \frac{4\tau_{N,1}^{e,B}}{1 - \Gamma_{N,N-1}^{e,B} e^{-j2\gamma_N^B d_N^B}}, \\
T_{2,2}^{L} &= \frac{2\left(1 + \Gamma_{N,N-1}^{e,B} e^{-j2\gamma_N^B d_N^B}\right)}{1 - \Gamma_{N,N-1}^{e,B} e^{-j2\gamma_N^B d_N^B}}, \\
T_{2,2}^{R} &= \frac{2\left(1 + \Gamma_{P,P-1}^{e,C} e^{-j2\gamma_p^C d_p^C}\right)}{1 - \Gamma_{P,P-1}^{e,C} e^{-j2\gamma_p^C d_p^C}}.
\end{aligned} \tag{5.20}$$



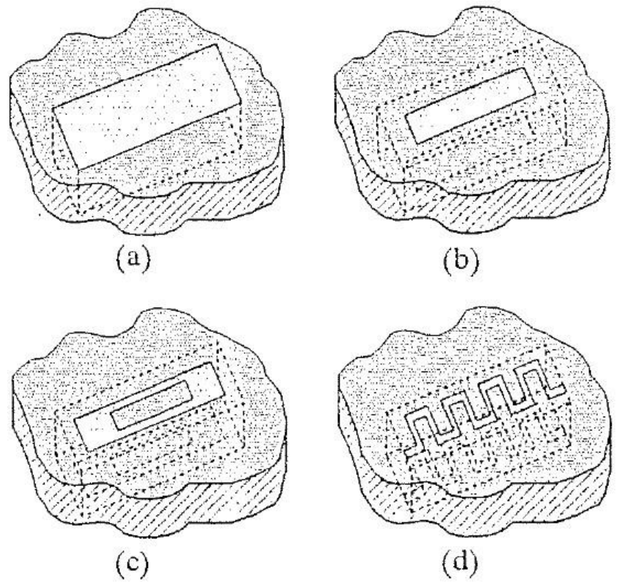


FIGURE 5.7 Some possible rectangular elements for thick-screen FSS applications.

### 5.1.4 Rectangular-Element Thick-Screen FSS

To analyze the thick-screen FSS with rectangular elements, we need to compute the inner products shown in (5.17) and apply them to the matrix solution. Figure 5.7 shows some possible rectangular-element configurations that can be considered for a thick-screen FSS. The configuration shown in Figure 5.7(b), where the rectangular element has rectangular irises at either end as defined in Figure 5.8, will be considered here. To solve this problem, we must compute the coupling between Floquet modes and magnetic current modes in the aperture and the coupling between magnetic current modes in the aperture and rectangular waveguide modes.

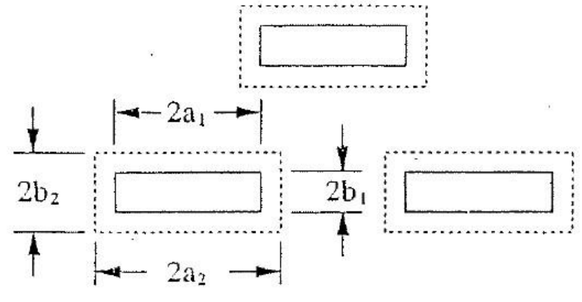


FIGURE 5.8 Geometry of element shown in Figure 5.7(b).

The magnetic current modes, $\mathbf{e}_p^1$ and $\mathbf{e}_q^2$ in (5.17), actually have double indices here and are divided into transverse electric (TE) and transverse magnetic (TM) modes. For example, $\mathbf{M}_{S1}^L$ is

$$\mathbf{M}_{S1}^L = \sum_p A_p \mathbf{e}_p^1 = \sum_p A_p^{\mathrm{TE}} \mathbf{e}_{1p}^1 + \sum_p A_p^{\mathrm{TM}} \mathbf{e}_{2p}^1,$$

where $p$ refers to the double-index waveguide modes. For simplicity, the left and right apertures are assumed identical, which may not be true in general. For this case the TE magnetic current modes, $\mathbf{e}_{1qs}$, are

$$\mathbf{e}_{1qs} = \frac{-\sqrt{\epsilon_q \epsilon_s}}{\sqrt{q^2 b_1/a_1 + s^2 a_1/b_1}} \left\{ \hat{x} \frac{q}{2a_1} \sin\left[\frac{q\pi x}{2a_1} + \frac{q\pi}{2}\right] \cos\left[\frac{s\pi y}{2b_1} + \frac{s\pi}{2}\right] + \hat{y} \frac{s}{2b_1} \cos\left[\frac{q\pi x}{2a_1} + \frac{q\pi}{2}\right] \sin\left[\frac{s\pi y}{2b_1} + \frac{s\pi}{2}\right] \right\},$$

where $q = 0, 1, 2, \ldots$, $s = 0, 1, 2, \ldots$ excluding $q = s = 0$ and $\epsilon_q = 1$ if $q = 0$ and $\epsilon_q = 2$ otherwise. Note that $q$ and $s$ are indices precisely like waveguide-mode indices. The TM magnetic current modes, $\mathbf{e}_{2qs}$, are

$$\mathbf{e}_{2qs} = \frac{2}{\sqrt{q^2 b_1/a_1 + s^2 a_1/b_1}} \left\{ -\hat{x} \frac{s}{2b_1} \sin\left[\frac{q\pi x}{2a_1} + \frac{q\pi}{2}\right] \cos\left[\frac{s\pi y}{2b_1} + \frac{s\pi}{2}\right] + \hat{y} \frac{q}{2a_1} \cos\left[\frac{q\pi x}{2a_1} + \frac{q\pi}{2}\right] \sin\left[\frac{s\pi y}{2b_1} + \frac{s\pi}{2}\right] \right\},$$

where $q = 1, 2, 3, \ldots$, $s = 1, 2, 3, \ldots$.

The vector waveguide modes in the waveguide region of the thick-screen FSS are very similar to the magnetic current modes. In (5.17), $\mathbf{h}_n^{WG}$ represent the waveguide modes, but, like the magnetic current modes, here they actually have double indices and are divided into TE and TM modes. The TE magnetic-field waveguide modes, $\mathbf{h}_{1pc}^{WG}$, are

$$\mathbf{h}_{1pc}^{WG} = \frac{-\sqrt{\epsilon_p \epsilon_c}}{\sqrt{p^2 b_2/a_2 + c^2 a_2/b_2}} \left\{ \hat{x} \frac{p}{2a_2} \sin\left[\frac{p\pi x}{2a_2} + \frac{p\pi}{2}\right] \cos\left[\frac{c\pi y}{2b_2} + \frac{c\pi}{2}\right] + \hat{y} \frac{c}{2b_2} \cos\left[\frac{p\pi x}{2a_2} + \frac{p\pi}{2}\right] \sin\left[\frac{c\pi y}{2b_2} + \frac{c\pi}{2}\right] \right\},$$

where $p = 0, 1, 2, \ldots$, $c = 0, 1, 2, \ldots$ excluding $p = c = 0$, and the TM



magnetic-field waveguide modes are

$$\mathbf{h}_{2pc}^{WG} = \frac{2}{\sqrt{p^2 b_2/a_2 + c^2 a_2/b_2}} \left\{ \hat{x} \frac{c}{2b_2} \sin\left[\frac{p\pi x}{2a_2} + \frac{p\pi}{2}\right] \cos\left[\frac{c\pi y}{2b_2} + \frac{c\pi}{2}\right] - \hat{y} \frac{p}{2a_2} \cos\left[\frac{p\pi x}{2a_2} + \frac{p\pi}{2}\right] \sin\left[\frac{c\pi y}{2b_2} + \frac{c\pi}{2}\right] \right\},$$

where $p = 1, 2, 3, \ldots$, and $c = 1, 2, 3, \ldots$.

The Floquet modes, represented by $\mathbf{h}_m^F$ in (5.17), also have double indices and are divided into TE and TM modes. The TE Floquet-mode magnetic field is

$$\mathbf{h}_{1mn}^F = \frac{1}{\sqrt{S_\alpha}} \left( \hat{x} \frac{k_x^{mn}}{k_r^{mn}} + \hat{y} \frac{k_y^{mn}}{k_r^{mn}} \right) e^{-j(xk_x^{mn} + yk_y^{mn})},$$

where

$$S_\alpha = db \sin \alpha,$$

$$k_r^{mn} = \sqrt{(k_x^{mn})^2 + (k_y^{mn})^2},$$

$$k_x^{mn} = k_0 T_x - \frac{2\pi m}{b},$$

$$k_y^{mn} = k_0 T_y - \left( \frac{2\pi n}{d \sin \alpha} - \frac{2\pi m}{b \tan \alpha} \right),$$

and $T_x$ and $T_y$ are the direction cosines that define the angle of incidence for the plane wave incident on the thick-screen FSS. The parameters $d$, $b$, and $\alpha$ are defined by the grid in Figure 5.2. Similarly, the TM modes are

$$\mathbf{h}_{2mn}^F = \frac{1}{\sqrt{S_\alpha}} \left( -\hat{x} \frac{k_y^{mn}}{k_r^{mn}} + \hat{y} \frac{k_x^{mn}}{k_r^{mn}} \right) e^{-j(xk_x^{mn} + yk_y^{mn})}.$$

The coupling integrals that must be solved to achieve a solution to (5.17) are $\langle \mathbf{e}_{1qs}, \mathbf{h}_{1mn}^F \rangle$, $\langle \mathbf{e}_{1qs}, \mathbf{h}_{2mn}^F \rangle$, $\langle \mathbf{e}_{2qs}, \mathbf{h}_{1mn}^F \rangle$, $\langle \mathbf{e}_{2qs}, \mathbf{h}_{2mn}^F \rangle$, $\langle \mathbf{e}_{1qs}, \mathbf{h}_{1pc}^{WG} \rangle$, $\langle \mathbf{e}_{1qs}, \mathbf{h}_{2pc}^{WG} \rangle$, $\langle \mathbf{e}_{2qs}, \mathbf{h}_{1pc}^{WG} \rangle$, and $\langle \mathbf{e}_{2qs}, \mathbf{h}_{2pc}^{WG} \rangle$. These integrals can be solved numerically over the aperture region or in closed form for a more efficient formulation of the problem. The Appendix describes the details of these reaction integrals for the specific rectangular-element thick-screen FSS geometry shown in Figure 5.8. Once these integrals are solved, the system of equations in (5.18) is easily solved by conventional methods to yield the unknown $A_i$ and $B_i$ coefficients. Note that the matrix in (5.18) is only as large as the number of current modes needed to represent accurately the

field in the aperture, which is usually small since full-domain basis functions are used. Typically, less than 20 modes are used at each aperture, so the matrix is solved very quickly. The majority of computation time occurs when filling the elements of the matrix with results of the inner-product calculations. For this reason, any coupling integrals that are not solved in closed form add greatly to the overall computation time of a computer program written to analyze this problem.

### 5.1.5 Circular-Element Thick-Screen FSS

Figure 5.9 shows several possible elements for application in a circular-element thick-screen FSS. The element in Figure 5.9(a) is a simple circular waveguide through hole, which is sometimes referred to as a puck plate because of the high dielectric ceramic pucks that are often used to load the waveguide. Circular waveguide modes are used to represent the magnetic currents in the apertures and the fields inside the screen itself. Similarly, the element in Figure 5.9(b) is a coaxial waveguide through hole in which coaxial waveguide modes are used to represent the fields in the screen [5]. The elements in Figures 5.9(c) and 5.9(d) compose "the artificial puck plate" bandpass radome [6]. In Figure 5.9(c), coaxial waveguide modes are used to represent the magnetic currents in the apertures, and circular waveguide modes are used to represent the fields inside the screen. Circular and coaxial waveguide-mode definitions can be found in Marcuvitz [7].

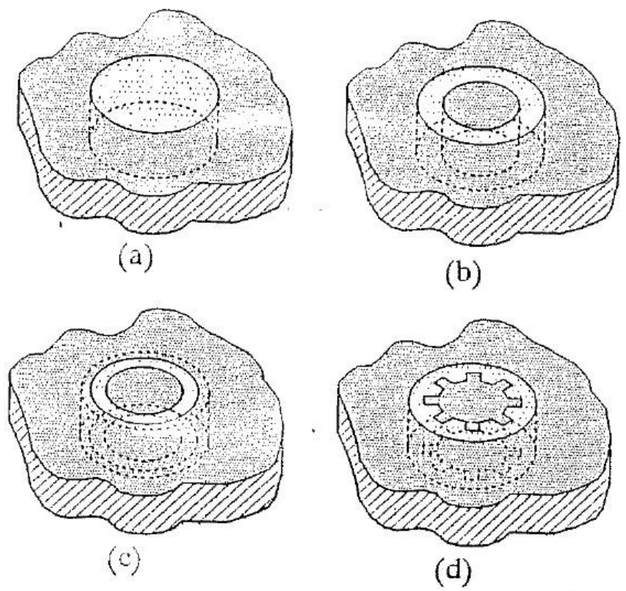


FIGURE 5.9 Some possible circular elements for thick-screen FSS applications.



***Puck Plate Bandpass Radome*** Figure 5.10 shows the geometry of a thick-screen FSS similar to Figure 5.9(a) where no irises are present, and circular waveguide modes are used to represent the magnetic currents at the apertures. Figure 5.11 shows the predicted transmission response of this thick-screen bandpass radome at several incidence angles for TE and TM polarizations. These predictions were generated by a numerical analysis code that employs the analysis techniques of this chapter. Note that the $Q$ of this design is fairly high, but it can be adjusted by varying the dielectric constant of the load material, the plate thickness, and the hole diameter. Note also that the passband resonance shifts with scan angle and with incident polarization and that there is no flat passband region because the input impedance to the FSS varies with incidence angle and polarization. This behavior is typical of this type of thick-screen FSS (both circular element and rectangular element) when no irises are used in the apertures and no dielectrics are added to the outside of the conductive thick-screen region to help counteract the effects of the varying input impedance. Because the passband of this thick-screen radome is not stable with scan angle, it has limited applications where wide scan ability and wide bandwidth are not required.

***Iris-Loaded Circular Waveguide Element — The Artificial Puck Plate Radome*** Figure 5.12 shows the geometry of a Ka-band artificial puck plate (APP) thick-screen bandpass radome, like that shown in Figure 5.9(c), where irises are included in both apertures and dielectric sheets have been added to the exterior to aid in stabilizing scan performance. Figure 5.13 shows a composite of transmission and reflection predictions from 0° to 70° off normal incidence. The passband remains stable centered around 35 GHz, and reflection

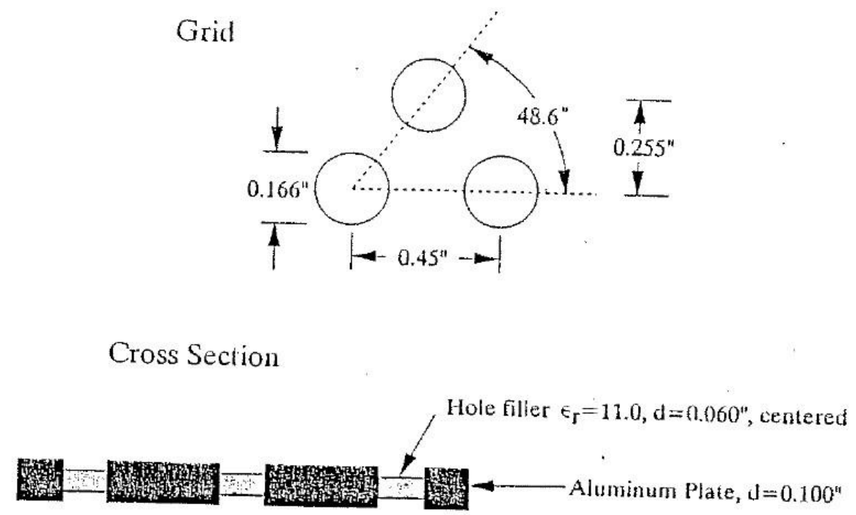


FIGURE 5.10 Geometry of a Ku-band puck plate.

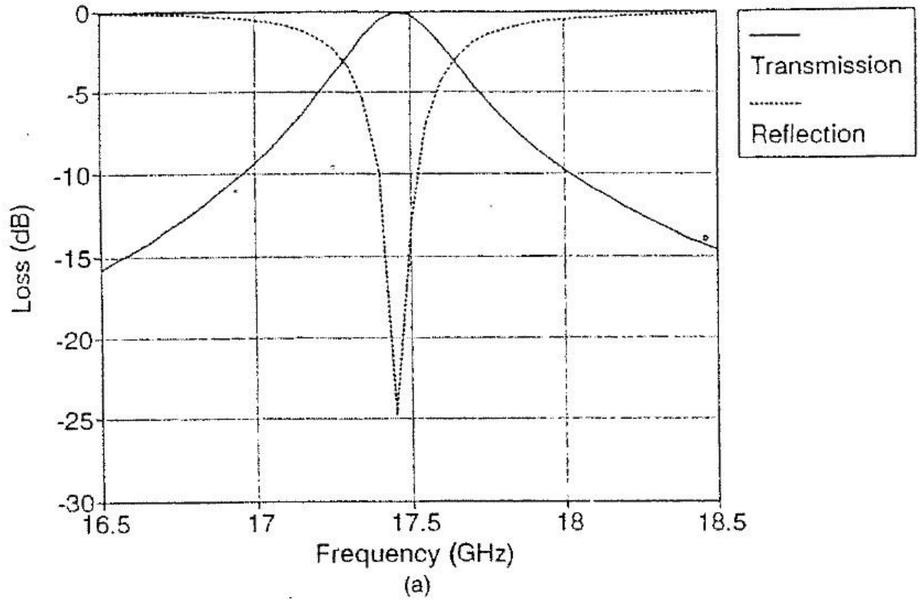


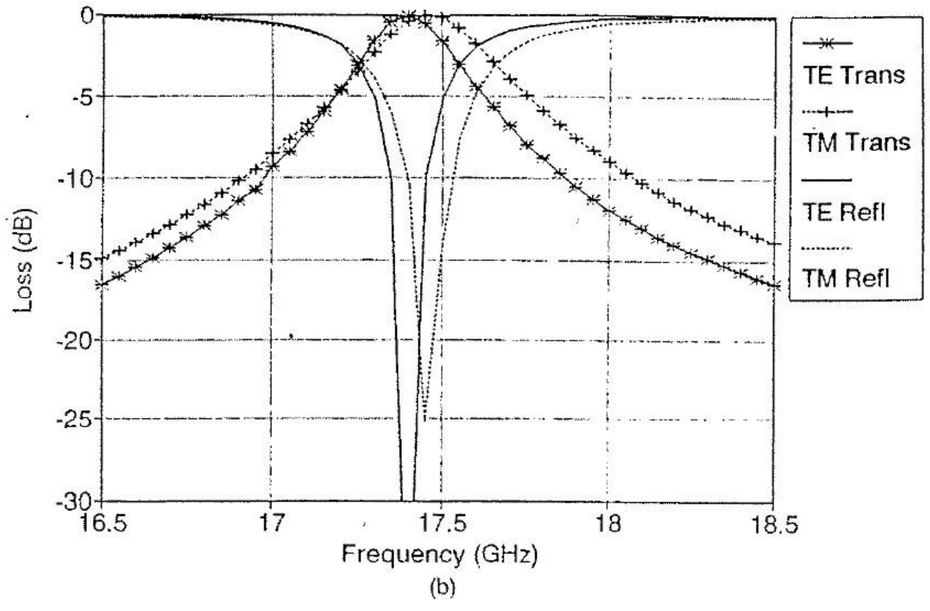


FIGURE 5.11 Performance of the Ku-band puck plate shown in Figure 5.10: (a) normal incidence; (b) $\phi = 0°, \theta = 30°$; (c) $\phi = 0°, \theta = 50°$; (d) $\phi = 0°, \theta = 70°$.



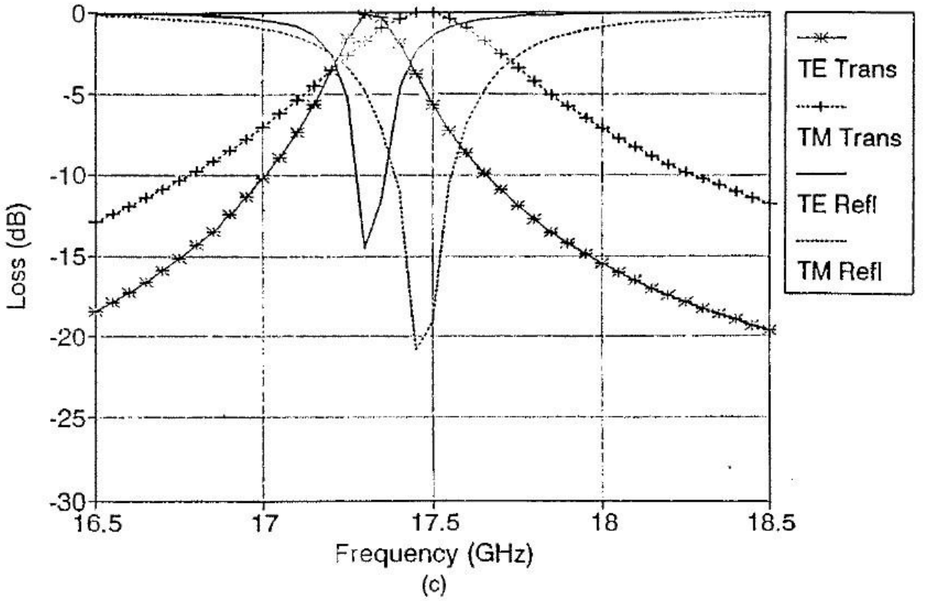


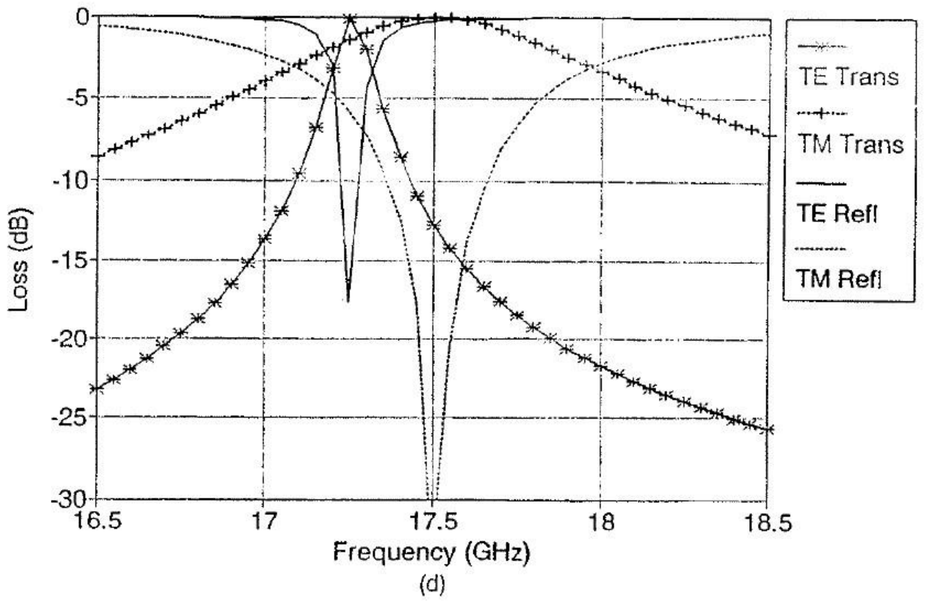


FIGURE 5.11 (*Continued*)

loss is very low. This performance is ideally suited for applications involving a wide-angle scanning antenna behind a bandpass radome. Note also that the $Q$ of this FSS is not extremely high but meets the requirements for which this radome was designed. The $Q$ can be easily adjusted by changing the dielectric constant of the load material, but higher $Q$s yield tighter tolerances and more difficult fabrication techniques. Figure 5.14 shows an example of the

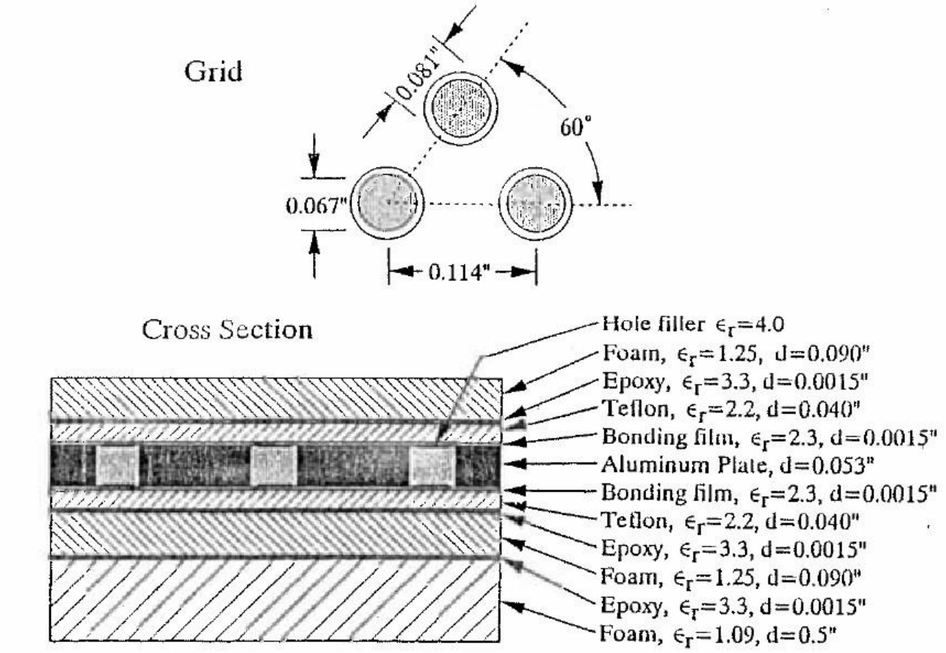


**FIGURE 5.12** Grid and element geometry of a Ka-band artificial puck plate radome.

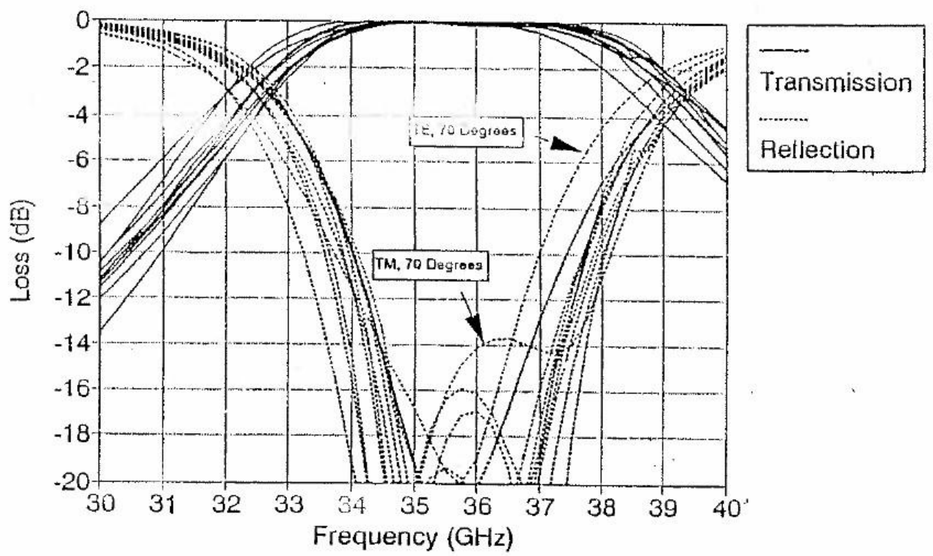


**FIGURE 5.13** Predicted transmission and reflection of the APP radome shown in Figure 5.12 at 0°, 30°, 40°, 50°, 60°, and 70° off normal incidence.



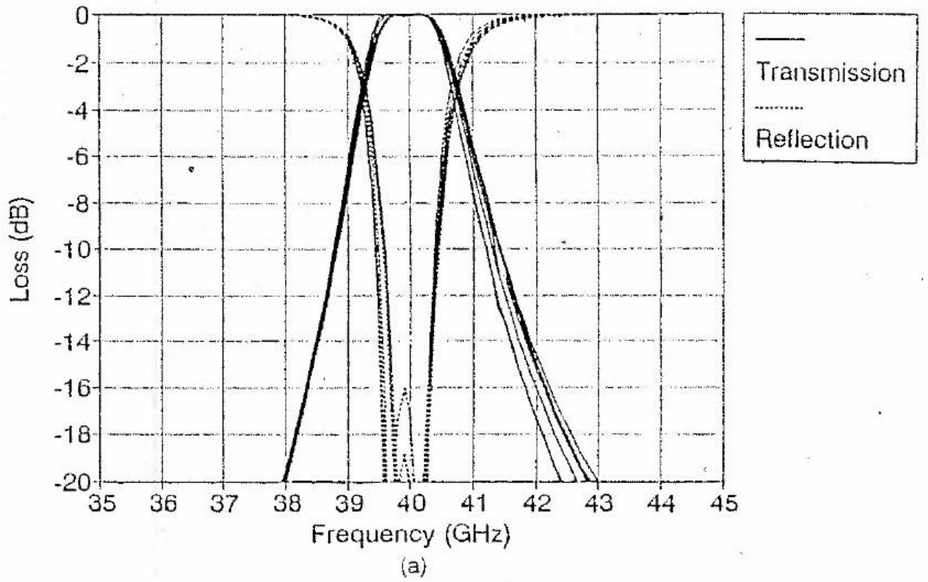


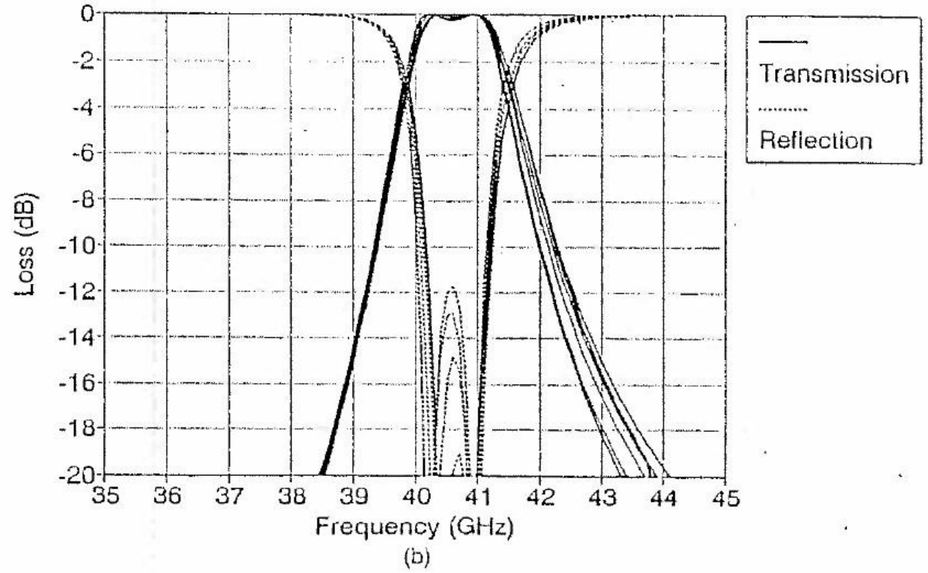


**FIGURE 5.14** Predicted transmission and reflection of a high-$Q$ APP bandpass radome at 0°, 30°, 40°, 50°, and 60° off normal incidence: (a) nominal design; (b) performance with 0.5-mil smaller radius patches that form the irises at either end of the waveguide section of the FSS.

sensitivity of a high-$Q$ APP radome design to an error in the iris etching. In Figure 5.14(b), the patch that forms the iris is 0.5 mil smaller in radius than that used to generate Figure 5.14(a). This relatively small error, which is within state-of-the-art etching processes, yields a radome that may not be usable. This sensitivity is typical of any high-$Q$ bandpass radome.

Figure 5.15 shows an APP bandpass radome with the parameters defined in Figure 5.12. The aperture region in this radome contains over 50,000 holes and is more than 4 ft$^2$. Construction of the radome began with drilling holes in an aluminum plate of the proper thickness. This simple drilling operation was performed efficiently with a numerically controlled machine. After drilling, the holes in the plate were filled simultaneously with a pourable dielectric, which is essential for this design to be manufacturable. The dielectric constant of the pourable mixture can be varied to almost any value to suit the electrical design. Much work was done with this dielectric to ensure that it did not shrink and fall out of the holes during the cure process. After the holes were filled with dielectric, copper foil was laminated to both sides of the plate. This was then etched to yield circular patches that were concentrically located with respect to the filled holes in the aluminum plate, thus forming the coaxial aperture of the APP radome. Dielectric sheets of the proper thickness were subsequently bonded to the exterior of the plate to form the complete prototype radome.

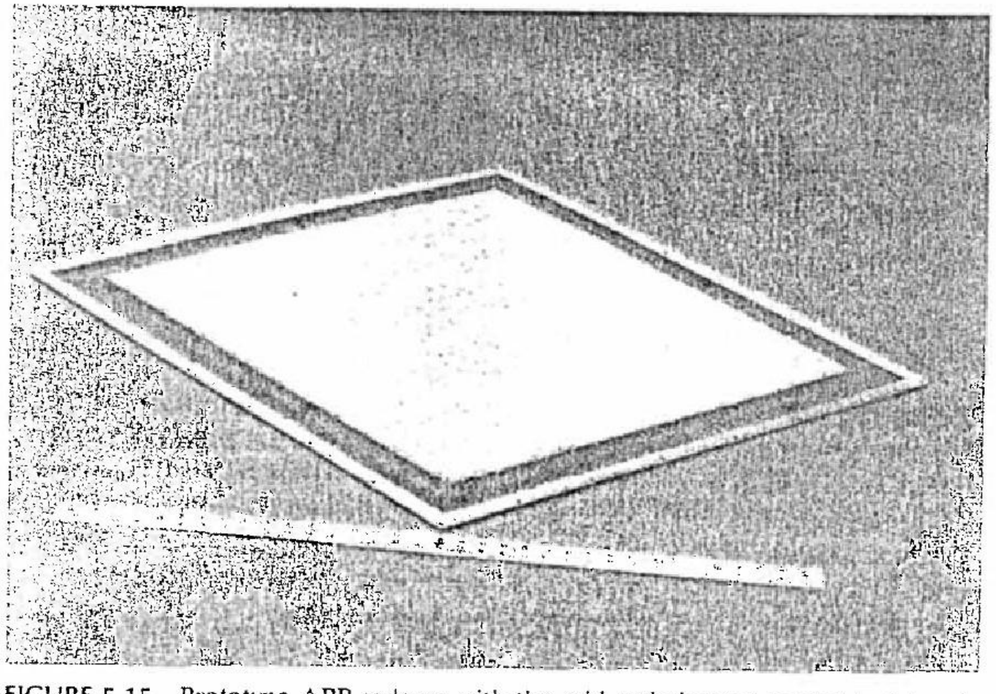

FIGURE 5.15 Prototype APP radome with the grid and element geometry shown in Figure 5.12.



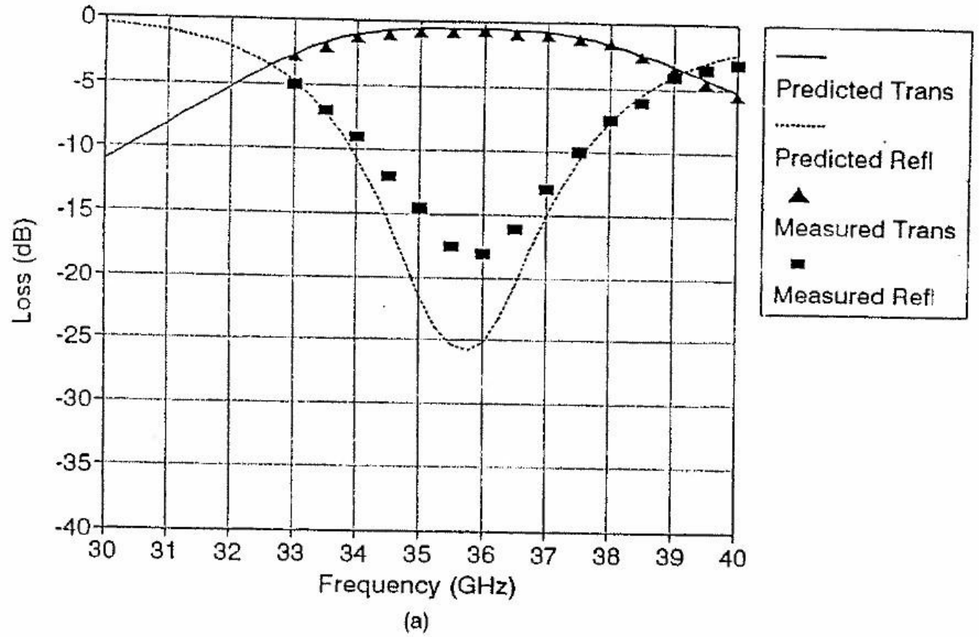


(a)

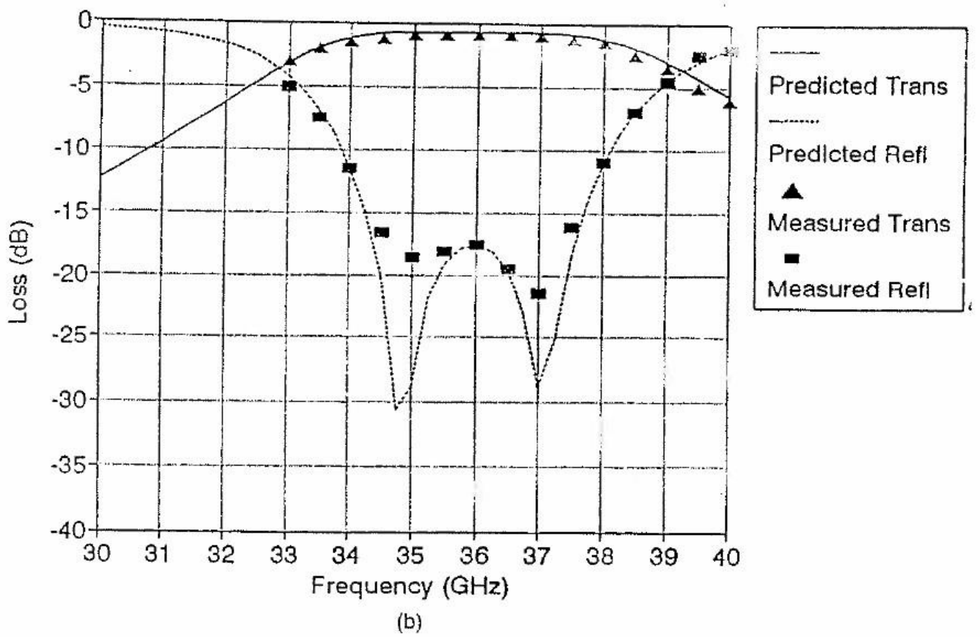


(b)

FIGURE 5.16 Typical predicted and measured transmission and reflection of the Ka-band APP radome shown in Figure 5.15: (a) 15° off normal incidence, TE polarization; (b) 60° off normal, TM polarization.

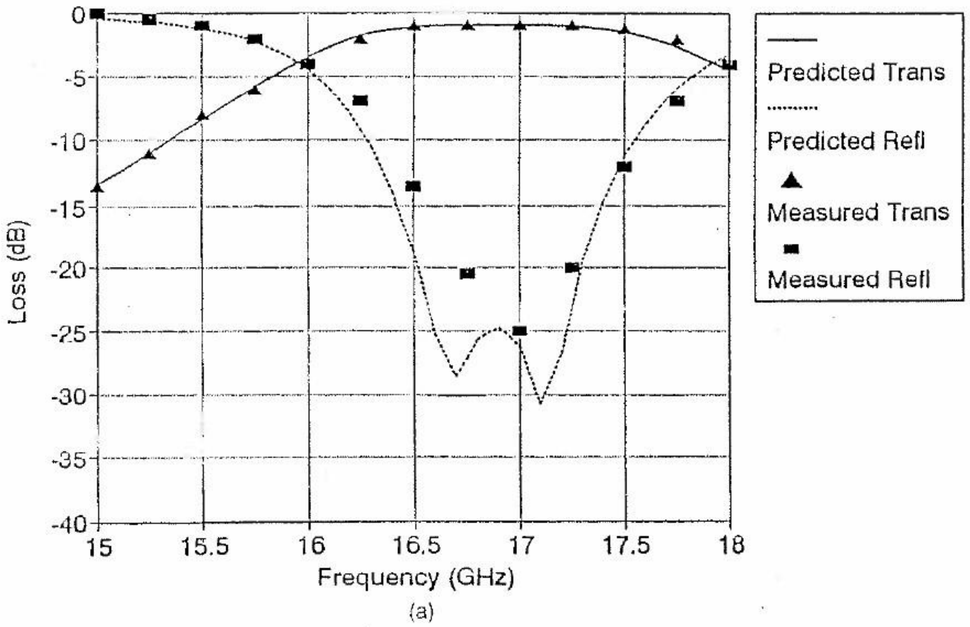


**FIGURE 5.17** Typical predicted and measured transmission and reflection of a Ku-band APP radome: (a) 30° off normal, TE polarization, (b) 60° off normal, TM polarization.



Several Ka- and Ku-band APP radomes were fabricated and measured to compare their transmission and reflection properties to predictions generated by a numerical analysis computer code. Figure 5.16 shows predicted and measured transmission and reflection plots of the Ka-band radome with the geometry of Figure 5.12. Figure 5.17 shows measured and predicted performance of a Ku-band APP radome. The predictions agree very well with the measurements.

***Antenna Performance through an APP Radome*** Antenna patterns were measured through the radome shown in Figure 5.15 with the Ka-band flat-plate resonant antenna shown in Figure 5.18. Figure 5.19 shows several measured antenna patterns with and without the radome in place at several angles of incidence. The radome has about 1 dB of loss and has little effect on the antenna sidelobes, which is primarily due to the excellent reflection properties of this design.

Antenna patterns were also measured through a Ku-band APP by using a phased array. Figure 5.20 shows the array used, and Figure 5.21 shows the array with a Ku-band APP radome mounted in front of it. The radome and antenna were fixed in position with no attention given to proximity, and the various antenna patterns were measured as the antenna was commanded to

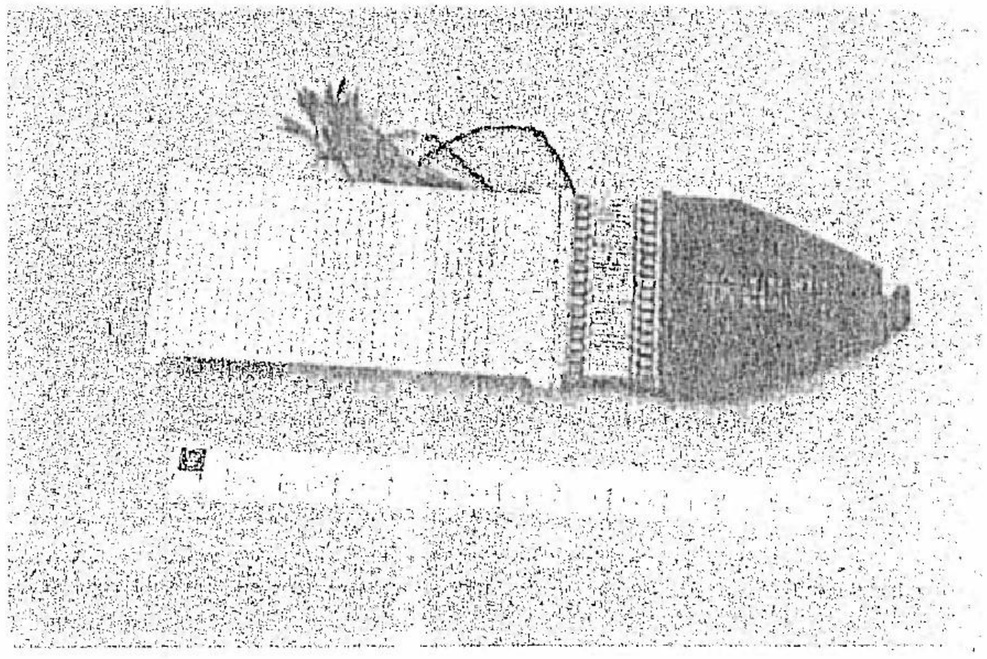

**FIGURE 5.18** Flat-plate antenna used to take patterns through the Ka-band APP radome shown in Figure 5.15.

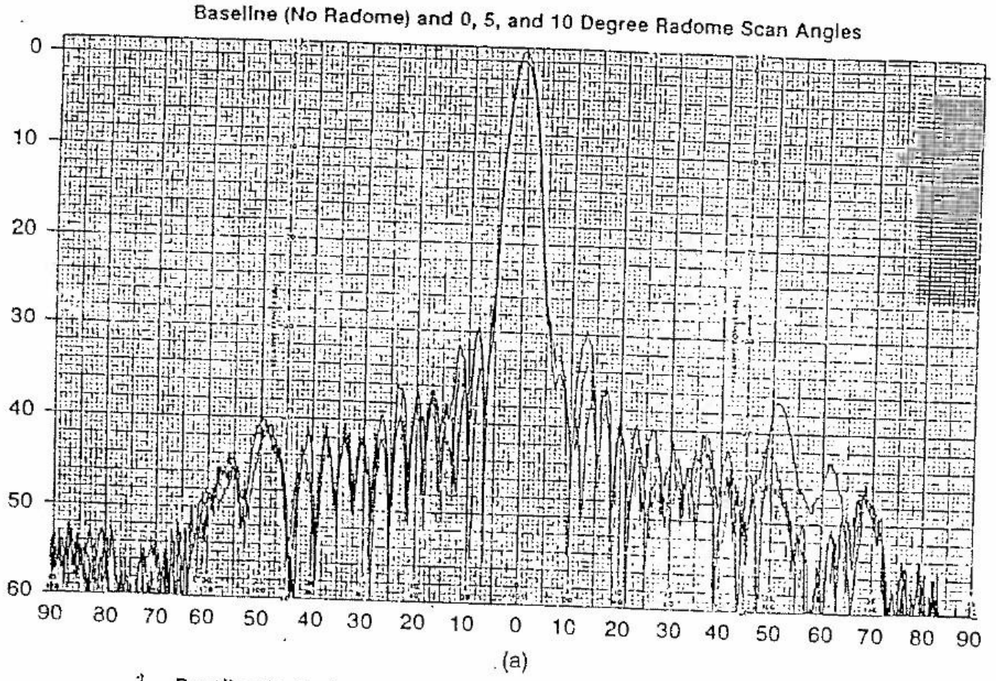


(a)

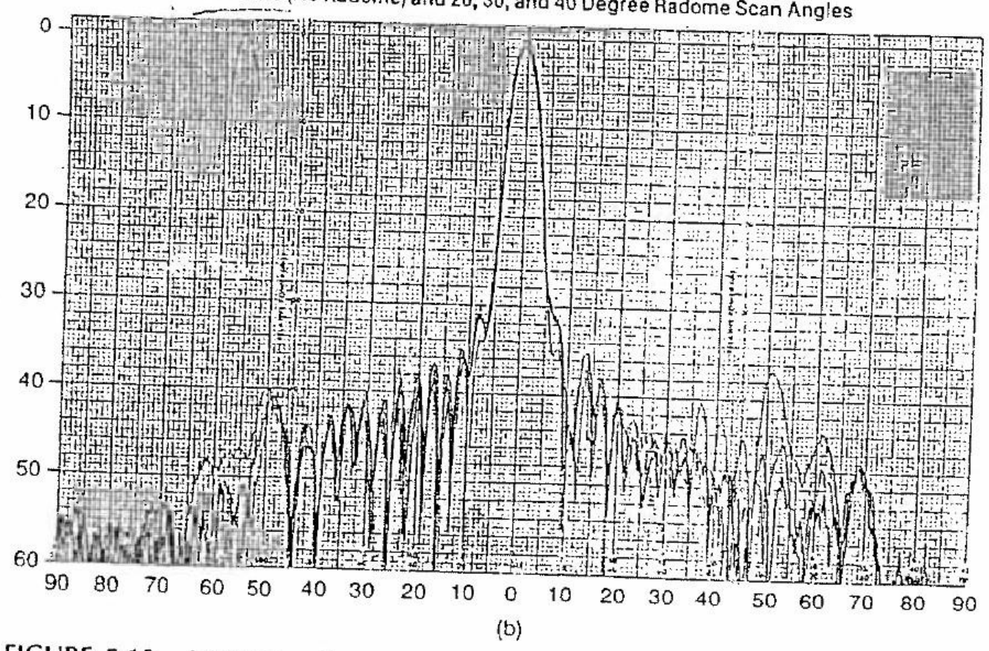


(b)

FIGURE 5.19 Antenna patterns measured through a Ka-band APP radome referenced to the baseline case where no radome is present: (a) 0°, 5°, and 10° incidence and baseline; (b) 20°, 30°, and 40° incidence and baseline; (c) 50°, 60°, and 70° incidence and baseline (note: for 70° incidence case, antenna is looking through a metal frame).



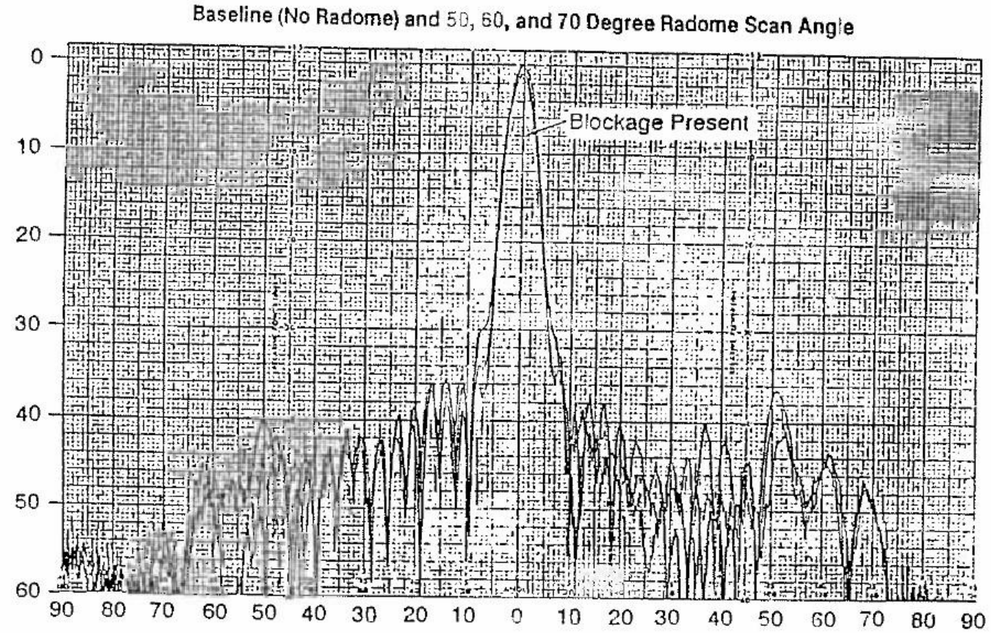


(c)

FIGURE 5.19 (*Continued*)

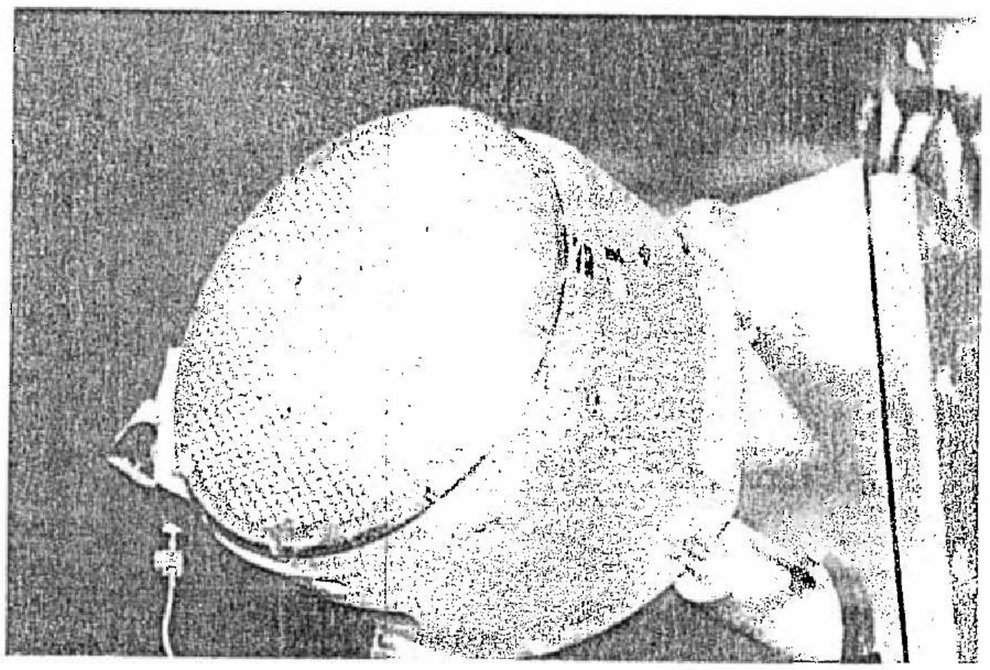

FIGURE 5.20 Phased array used to measure antenna patterns through a Ku-band APP radome.

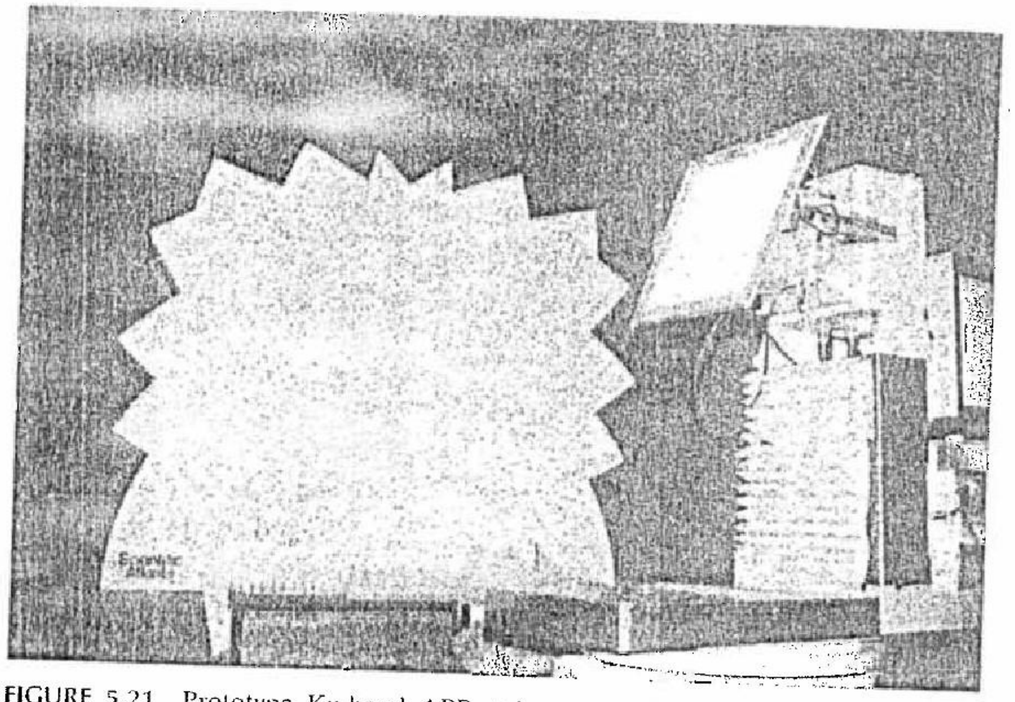

FIGURE 5.21 Prototype Ku-band APP radome mounted in front of the antenna shown in Figure 5.20.

different scan positions. Figure 5.22 shows a couple of these scan patterns compared to the antenna baseline. Again, the APP radome has little affect on the antenna pattern of this relatively-low-sidelobe antenna.

## 5.2 THIN-SCREEN FSS

The thin-screen FSS is composed of elements in a regular grid pattern that are formed in an electrically thin, conductive foil. Unlike the thick-screen FSS, in the analysis of the thin-screen FSS the conductive foil is assumed to be infinitesimally thin. Elements in the thin-screen FSS can have almost any conceivable shape. Figure 5.23 shows a few shapes commonly used in bandpass radome applications.

The thin screen is suspended on a planar dielectric and may appear similar to that in Figure 5.24, which shows two thin screens suspended in a planar dielectric sandwich. The etched element in this case is a crossed dipole. The thin-screen FSS is more widely used than the thick screen because it is simpler and easier to manufacture. It is also generally lighter, since it can be composed almost entirely of lightweight dielectric materials, thereby making it generally more suitable in lightweight aircraft and space-



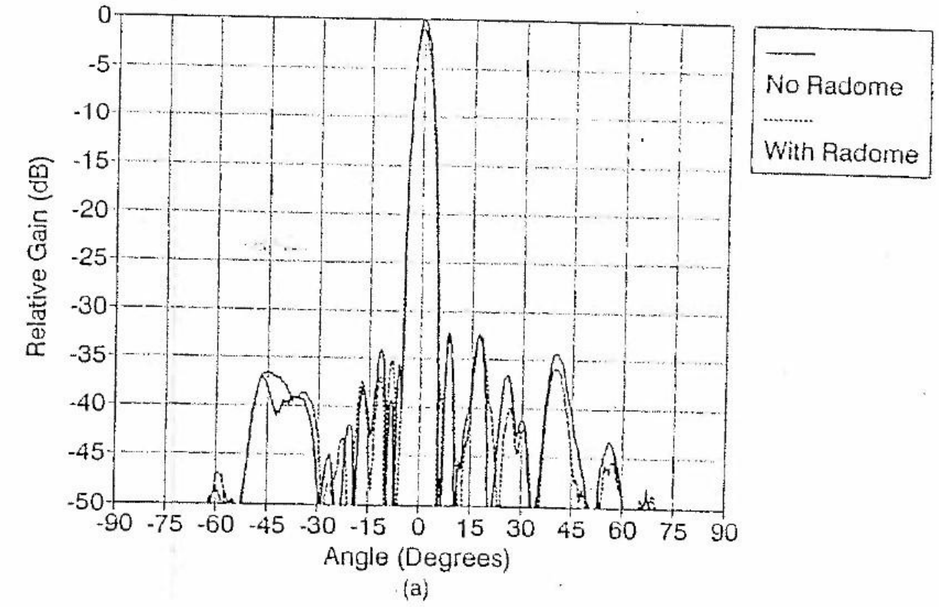


(a)

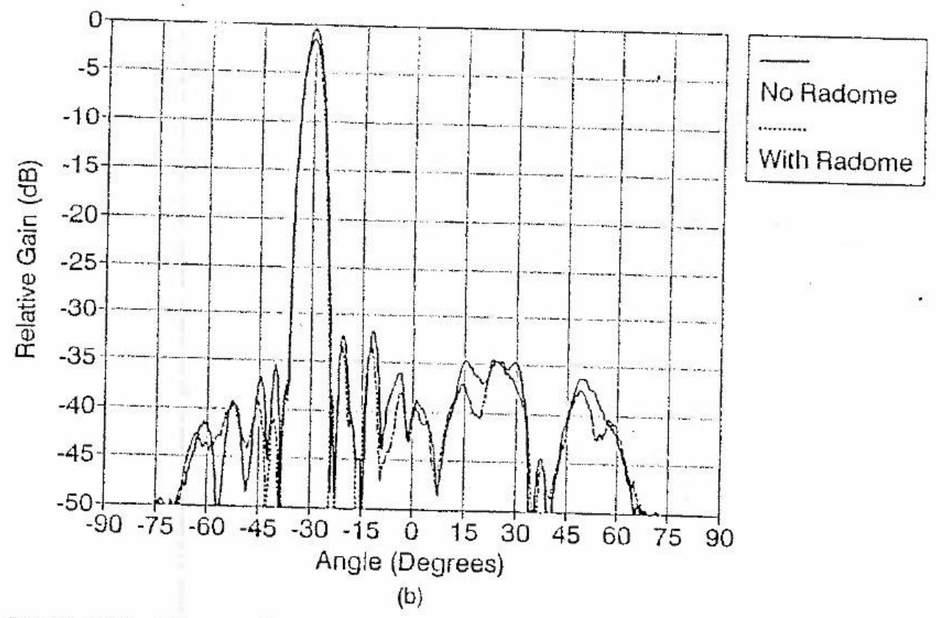


(b)

FIGURE 5.22 Measured patterns through a Ku-band APP radome, using the configuration shown in Figure 5.21, compared to the baseline pattern: (a) normal incidence; (b) 30° scan; (c) 50° scan.

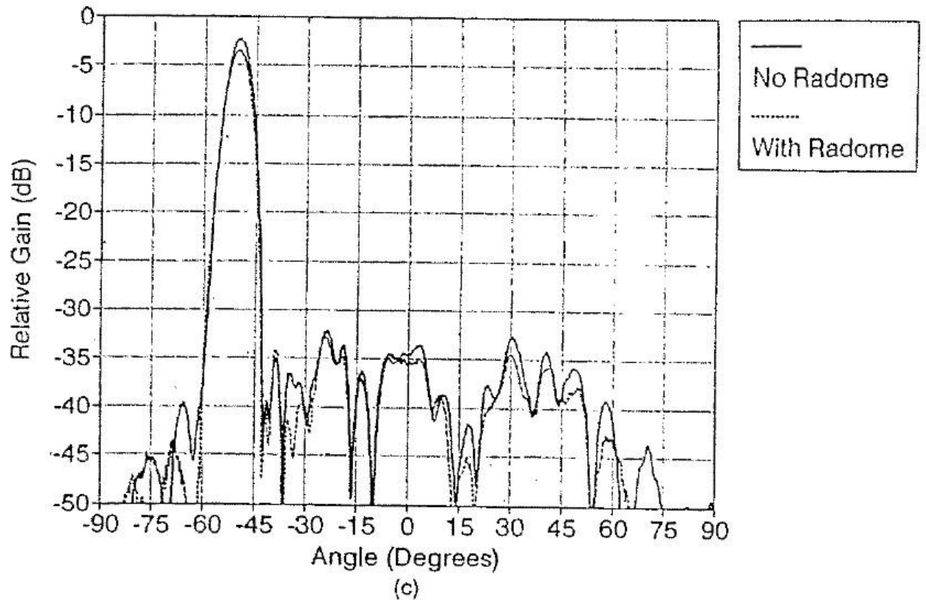


FIGURE 5.22 (*Continued*)

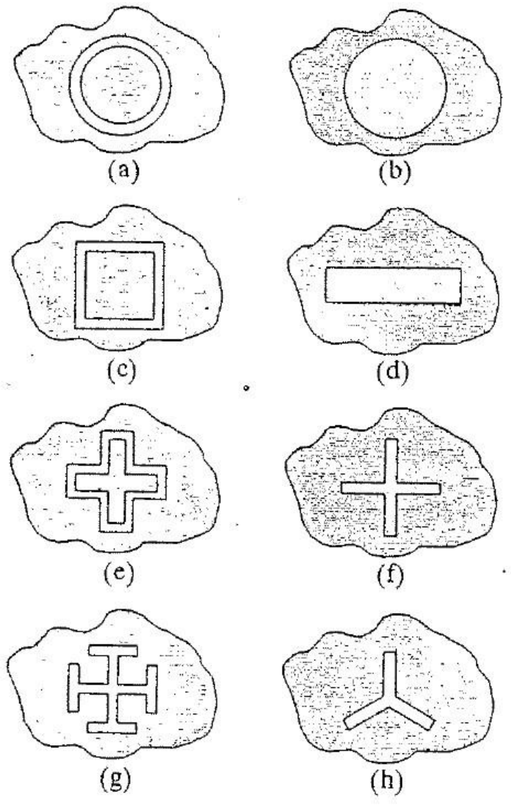


FIGURE 5.23 Some possible elements for use in thin-screen FSS applications.



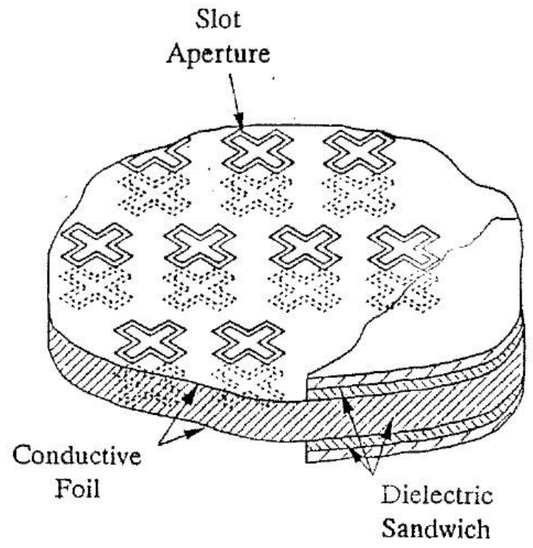


FIGURE 5.24 Typical two-thin-screen FSS showing etched elements and dielectric sandwich construction of this type of bandpass radome.

craft applications. However, the thick-screen FSS appears to have better bandpass stability as a function of scan angle; that is, as the incident angle deviates from normal, the passband of the FSS appears to shift from its nominal value more in a thin-screen FSS. Despite this drawback, thin-screen FSSs can be designed with very good scan stability characteristics in multi-screen designs, which together with low cost and ease of manufacture often make it the FSS of choice.

### 5.2.1 Thin-Screen FSS Analysis

The thin-screen FSS can be analyzed in precisely the same fashion as the thick-screen FSS. The thin-screen FSS can be composed of any number of screens, but here only the single- and two-screen FSS, which are most commonly used in bandpass radome applications, are considered.

***Single-Thin-Screen FSS*** Figure 5.25 shows the general geometry of a single-thin-screen FSS where every element is identical and arranged in a regular grid, as shown in Figure 5.2. As with the thick-screen FSS, multiple dielectric sheets are allowed on either side of the thin screen. Figure 5.26 shows the equivalent problem for analyzing the single-thin-screen FSS. This appears very similar to Figure 5.3 for the thick-screen FSS where the apertures are replaced with perfect conductors and sheets of magnetic current are placed on top of the conductor on both sides of the aperture. Again the problem is solved by enforcing continuity of the tangential electric and magnetic fields

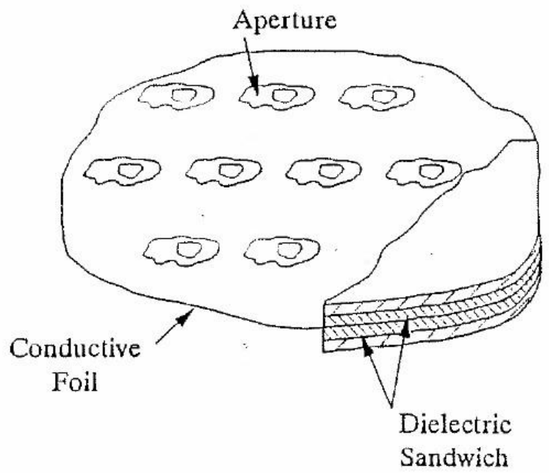


FIGURE 5.25 General single-thin-screen FSS geometry.

across the aperture of the FSS. Since only a single aperture is considered here, (5.1) alone applies to the single-thin-screen FSS.

The magnetic field to the left side of the FSS is given by (5.9) and is repeated here:

$$\begin{aligned}\mathbf{H}_T^{1L} &= \mathbf{H}_{\text{inc}}^{1L} + \mathbf{H}_{MS1}^{1L} \\ &= T_{\text{inc}}\mathbf{H}_{\text{inc}} - \sum_m Y_m^{MA}\frac{T_{1,1}^L}{2}\langle \mathbf{M}_{S1}^L, \mathbf{h}_m^F\rangle \mathbf{h}_m^F. \end{aligned} \tag{5.21}$$

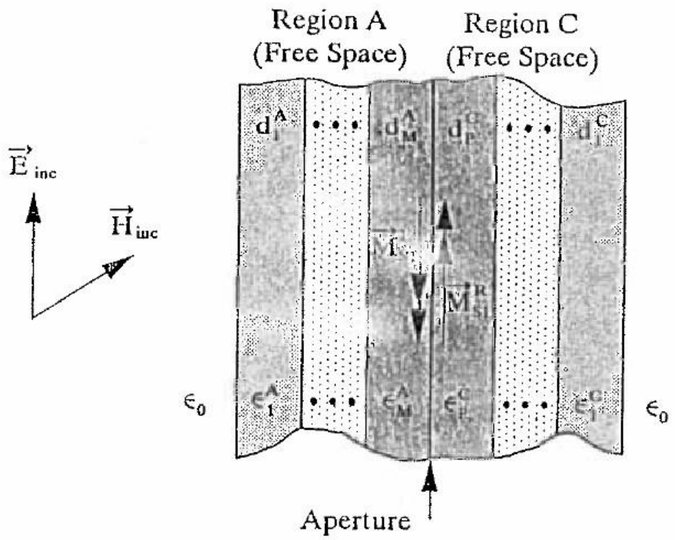


FIGURE 5.26 Equivalent problem used to analyze the transmission and reflection properties of the single-thin-screen FSS.



On the right side it is given by (5.14) with the exception of some notation changes:

$$\mathbf{H}_T^{1R} = -\sum_m Y_m^{PC}\frac{T_{1,1}^R}{2}\langle \mathbf{M}_{S1}^R, \mathbf{h}_m^F\rangle \mathbf{h}_m^F. \tag{5.22}$$

The variable definitions in (5.21) are precisely the same as in (5.9), including the $T$-factor, and the definitions in (5.22) are exactly the same as in (5.14). Combining (5.21) and (5.22), we obtain the system equation defining the single-thin-screen FSS:

$$\begin{aligned} T_{\text{inc}}\mathbf{H}_{\text{inc}} = &\sum_m Y_m^{MA}\frac{T_{1,1}^L}{2}\langle \mathbf{M}_{S1}^L, \mathbf{h}_m^F\rangle \mathbf{h}_m^F \\ &- \sum_m Y_m^{PC}\frac{T_{1,1}^R}{2}\langle \mathbf{M}_{S1}^R, \mathbf{h}_m^F\rangle \mathbf{h}_m^F. \end{aligned} \tag{5.23}$$

Following the same format as (5.17), we write this as

$$\begin{aligned} T_{\text{inc}}\langle \mathbf{e}_i^1, \mathbf{H}_{\text{inc}}\rangle^* = &\sum_p A_p \sum_m Y_m^{MA}\frac{T_{1,1}^L}{2}\langle \mathbf{e}_p^1, \mathbf{h}_m^F\rangle\langle \mathbf{e}_i^1, \mathbf{h}_m^F\rangle^* \\ &+ \sum_p A_p \sum_m Y_m^{PC}\frac{T_{1,1}^R}{2}\langle \mathbf{e}_p^1, \mathbf{h}_m^F\rangle\langle \mathbf{e}_i^1, \mathbf{h}_m^F\rangle^*, \end{aligned} \tag{5.24}$$

where variable definitions are the same as in (5.17), except $T_{1,1}^R$ in (5.24) is defined like $T_{2,2}^R$ in (5.17).

***Two-Thin-Screen FSS*** The two-thin-screen FSS analysis is identical to the thick-screen FSS analysis. Figure 5.24 shows the geometry of a two-thin-screen FSS that contains quadrapole elements. The equivalent problem for this FSS is identical to that in Figure 5.3 if the waveguide region in Figure 5.3 is removed and replaced with a free-space region. In fact, the system of equations generated for the thick-screen FSS in (5.17) applies directly to the two-layer thin-screen FSS simply by replacing the waveguide modes, $\mathbf{h}_n^{WG}$, by Floquet modes, $\mathbf{h}_m^F$. With this modification, (5.17) applies directly to the two-thin-screen FSS. The $T$-factors for the problem also remain identical and are given by (5.20).

As with the thick-screen FSS, the magnetic current modes in the aperture should be carefully chosen such that they easily represent the field in the aperture. Wu [8] describes a two-layer thin-screen bandpass radome that contains rectangular apertures like that shown in Figure 5.23(d). Following the analysis here, a natural choice of basis functions for the magnetic currents for these rectangular apertures could be rectangular waveguide modes. If, on the other hand, the apertures become narrow slots, such as

those in Figure 5.23(f), then one may choose to use some type of rooftop or piecewise sinusoidal basis function.

### 5.2.2 Thin-Screen FSS Performance

Pelton and Munk [9] describe a single-thin-screen FSS for bandpass radome applications. The FSS element is a tripole element, as shown in Figure 5.23(h), and the radome contains no dielectric matching sheets. Figure 5.27

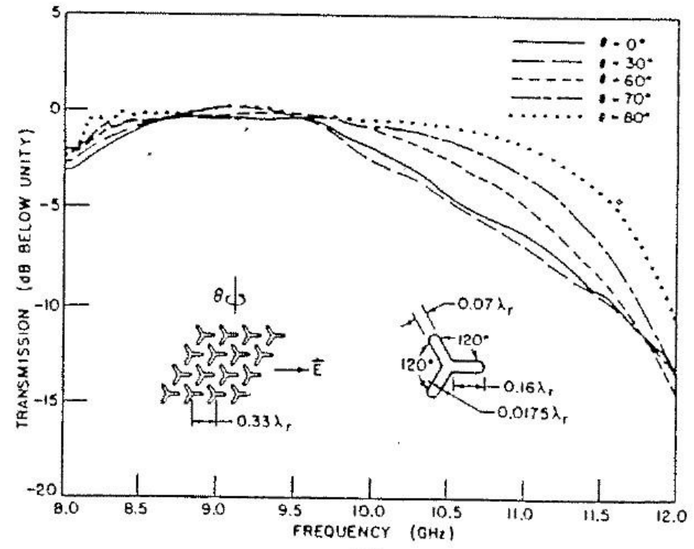


(a)

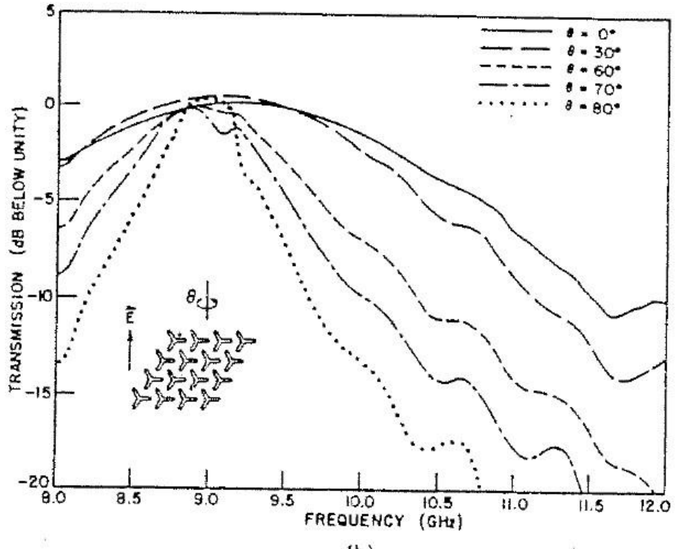


(b)

FIGURE 5.27 Measured flat-panel transmission vs. frequency characteristics for slotted metallic surface employed in metallic radome [9]: (a) $E$-plane; (b) $H$-plane.

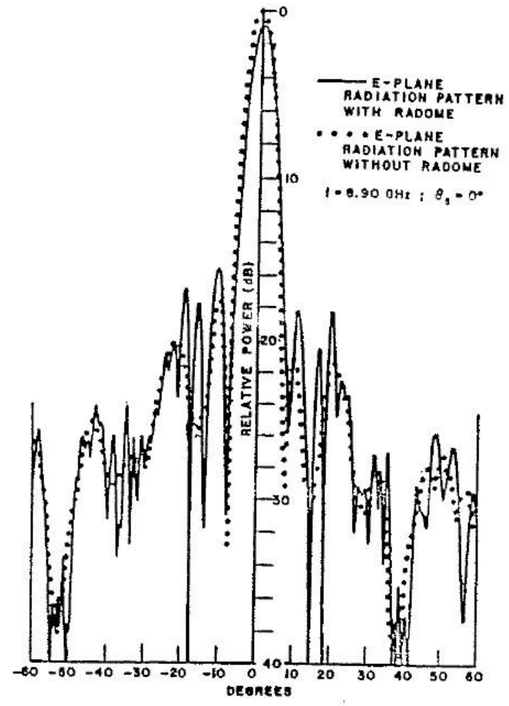


(a)

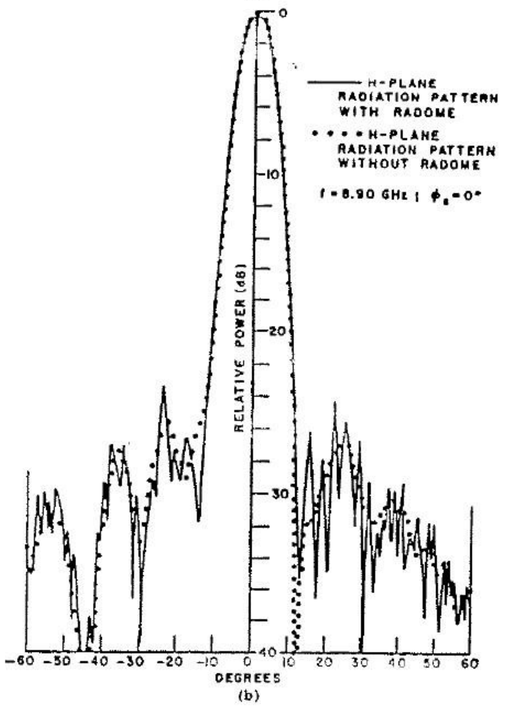


(b)

FIGURE 5.28 Measured radiation patterns of 14-in-diameter parabolic transmitting antenna, taken with and without radome present. In solid curves, radome and antenna axes are coincident, and both antenna and radome are rotated together [9]: (a) $E$-plane patterns; (b) $H$-plane patterns.

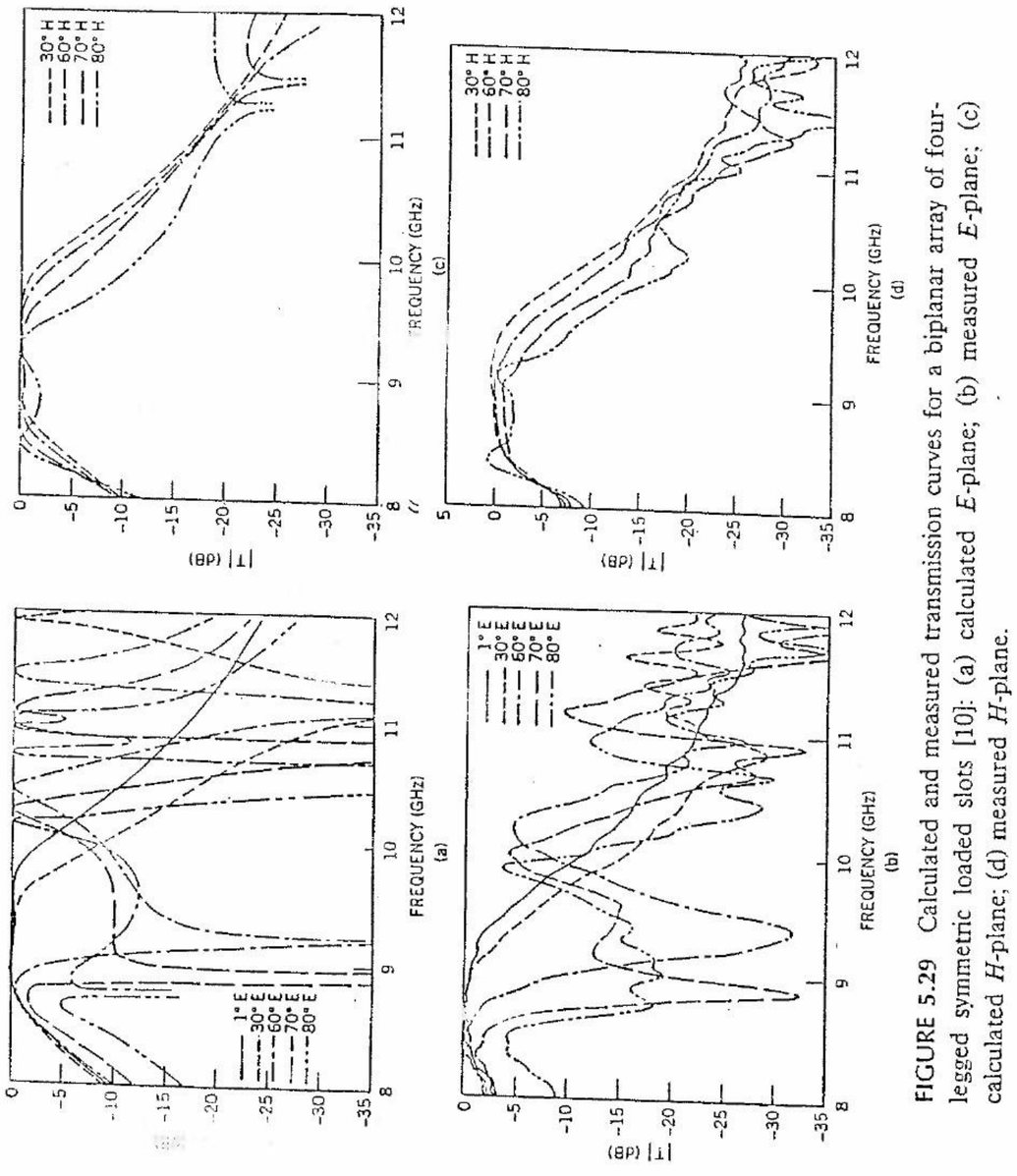


FIGURE 5.29 Calculated and measured transmission curves for a biplanar array of four-legged symmetric loaded slots [10]: (a) calculated *E*-plane; (b) measured *E*-plane; (c) calculated *H*-plane; (d) measured *H*-plane.





shows the measured *E*-plane and *H*-plane transmission of this bandpass radome design. The performance is very similar to that of the puck plate radome with no dielectric matching sheets (Figure 5.10), where the *H*-plane transmission is not highly stable with scan angle. Figure 5.28 shows some measured antenna patterns through a conical radome based on this design. Note that very little degradation to the patterns is incurred by introduction of the radome.

To achieve a wider passband that is more stable with scan angle and to achieve sharper skirts, one usually uses two-layer thin-screen FSSs [10]. These radomes have performance characteristics similar to those of the thick-screen APP radome described in Section 5.1.5. The design presented in Luebbers and Munk [10] utilizes the four-legged slot shown in Figure 5.23(e). Figure 5.29 shows predicted and measured *E*- and *H*-plane transmission at

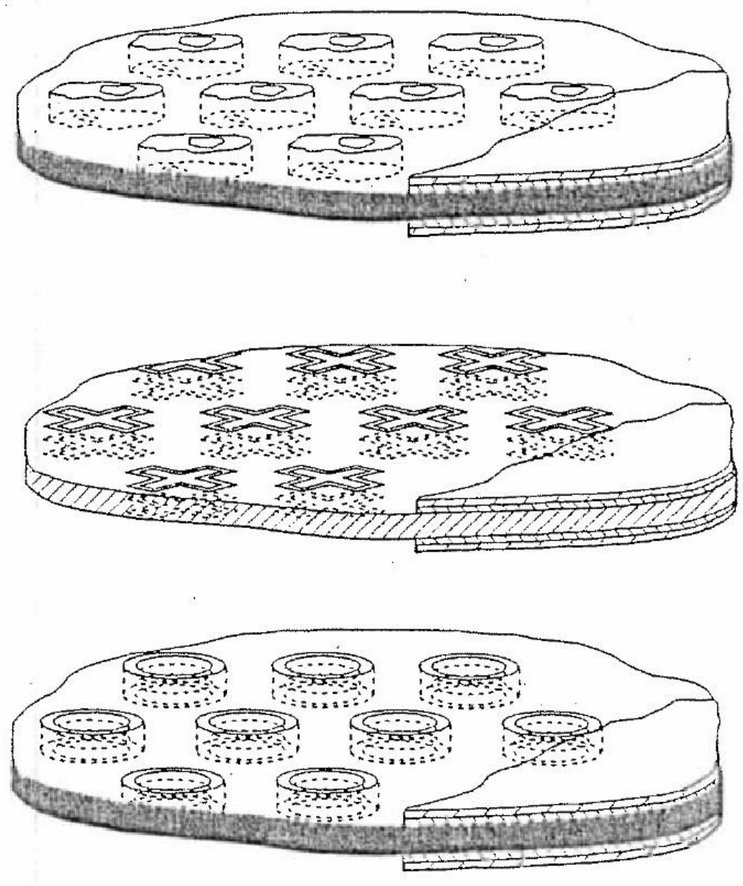

FIGURE 5.30 General arrangement of FSSs, including both thick- and thin-screen geometries.

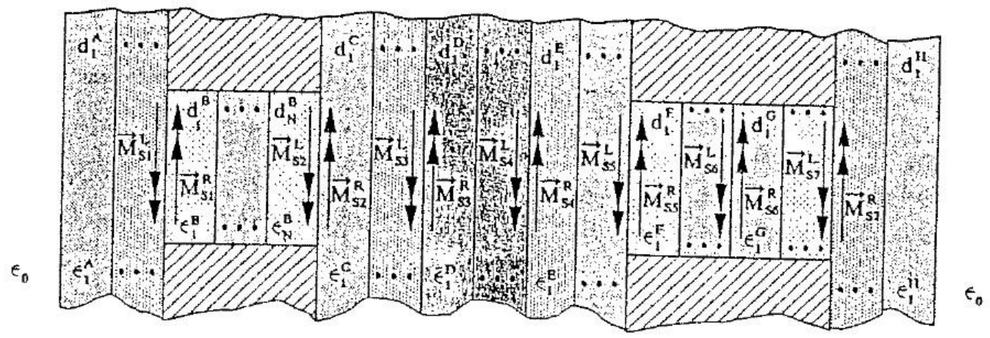

FIGURE 5.31 Equivalent problem used to analyze the FSS geometry shown in Figure 5.30.

various scan angles of a bandpass radome based on this two-screen, four-legged slot design. Note that much better scan performance than that in Figure 5.29 is possible through proper element design and proper design of the dielectric matching layers covering and separating the thin screens.

## 5.3 BANDPASS RADOME GENERALIZATION

Thick- and thin-screen FSSs can be combined and analyzed in any conceivable arrangement. Figure 5.30 shows one general arrangement. For the analysis in this chapter, it is required that the grids in each layer of the FSS be identical or an integer multiple of one another. Figure 5.31 shows the equivalent problem for analyzing the FSS in Figure 5.30. The problem is very easily broken up into regions that can each be analyzed by the methods of this chapter. The equations for this system are identical to those in (5.17), with the addition of one equation for each aperture added to the FSS. Fields will be expanded in Floquet modes in the free-space regions and in waveguide modes inside the thick screens. To solve the general problem one can generate a partitioned matrix, identical to that in (5.20). The number of submatrices corresponds exactly to the number of apertures in the FSS.

## 5.4 CONCLUSIONS AND RECOMMENDATIONS

Both thick-screen and thin-screen bandpass radomes are used in a variety of applications. Table 5.1 is a comparison of some general properties of thick-screen and thin-screen FSSs. In general, the thin-screen FSS is more widely used than the thick-screen FSS in bandpass radome applications because of its relative simplicity and ease of manufacture compared to the thick screen.



TABLE 5.1. Comparison of Thick-Screen and Thin-Screen Parameters

| Parameter | Thick Screen | Thin Screen |
|---|---|---|
| $Q$ of single screen | High | Low |
| Scan performance of single screen | Good | Fair |
| $Q$ of two screen (two irises in thick screen) | High | High |
| Scan performance of two screen (two irises in thick screen) | Very good | Very good |
| Physical characteristics | Moderately thick, heavy | Thin, light |
| Fabrication of flat and singly curved radomes | Moderate difficulty | Simple |
| Fabrication of doubly curved radomes | Very difficult | Difficult |
| Internal surface-wave performance | Excellent | Fair |
| Scattering performance | Excellent | Good |

Also, because the thin-screen radome is composed almost entirely of lightweight dielectric materials, it is generally lighter than thick-screen radomes, making it more suitable in lightweight aircraft and spacecraft applications. However, if the radome is required to have the best $Q$, scan performance, and scattering performance possible, then a thick-screen radome is probably required.

Because thin-screen radomes are most often composed of several screens to achieve a higher $Q$ and scan stability, surface waves can be supported between the screens, especially at discontinuities. These surface waves can degrade the performance of the antenna through the radome, in addition to causing other scattering problems. Special attention should be given to the multiple-thin-screen radome design to ensure that discontinuities are avoided —this includes element grid discontinuities that are often encountered when fabricating radomes with complex shapes. If the potential problems associated with the internal surface waves in a multiple-layer thin-screen FSS cannot be tolerated, then a single-thick-screen FSS with multiple irises is required. The multiple irises in the thick-screen FSS give equivalent performance to the multiple-layer thin-screen FSS, but because the irises all exist within the thick conductive screen no internal surface waves or the problems associated with them are possible.

Regardless of the type of FSS used in the bandpass radome, special attention is required in the initial radome design in order to achieve a

manufacturable design. An often-overlooked parameter in the radome design, which relates directly to its manufacturability, is the $Q$ of the FSS. If one is required to design a high-$Q$ radome with performance similar to that shown in Figure 5.14(a), then it will be extremely sensitive to manufacturing errors and tolerances will need to be extremely tight in order to yield a satisfactory radome. These tight tolerances will make the radome difficult to fabricate and extremely expensive. These difficulties will be encountered for both thick-screen and thin-screen radomes. To yield a practical design, the radome should have a moderate $Q$ that allows it to be manufactured using simple, conventional methods. The manufacturing sensitivities can be, and should be, checked via the electromagnetic analysis presented in this chapter, or some similar method, to ensure a robust, manufacturable radome design.

## REFERENCES


1. R. F. Harrington, *Time-Harmonic Electromagnetic Fields*, pp. 106–110. McGraw-Hill, New York, 1961.
2. C. A. Balanis, *Advanced Engineering Electromagnetics*, pp. 329–346. Wiley, New York, 1989.
3. C. Scott, *The Spectral Domain Method in Electromagnetics*. Artech House, Norwood, MA, 1989.
4. B. A. Munk, *A General Theory of Periodic Surfaces in a Stratified Dielectric Medium*. Ohio State University, Columbus, 1986.
5. A. Roberts and R. C. McPhedran, Bandpass grids with annular apertures. *IEEE Trans. Antennas Propag.* **AP-36**(5), 607–611 (1988).
6. R. G. Schmier, E. W. Lucas, and J. A. Bingham, Frequency selective radome. U.S. 5,140,338 (1992).
7. N. Marcuvitz, *Waveguide Handbook*, pp. 66–80. McGraw-Hill, New York, 1949.
8. T. K. Wu, High $Q$ bandpass structure for the selective transmission and reflection of high frequency radio signals. U.S. 5,103,241 (1992).
9. E. L. Pelton and B. A. Munk, A streamlined metallic radome. *IEEE Trans. Antennas Propag.* **AP-22**, 799–809, (1974).
10. R. J. Luebbers and B. A. Munk, Mode matching analysis of biplanar slot arrays. *IEEE Trans. Antennas Propag.* **AP-27**(3), 441–443 (1979).


## APPENDIX

### Reaction Integrals for a Rectangular-Element Thick-Screen FSS

To solve (5.17) for the rectangular-element thick-screen FSS geometry in Figure 5.8, the reaction integrals $\langle \mathbf{e}_{1qs}, \mathbf{h}^F_{1mn} \rangle$, $\langle \mathbf{e}_{1qs}, \mathbf{h}^F_{2mn} \rangle$, $\langle \mathbf{e}_{2qs}, \mathbf{h}^F_{1mn} \rangle$, $\langle \mathbf{e}_{2qs}, \mathbf{h}^F_{2mn} \rangle$, $\langle \mathbf{e}_{1qs}, \mathbf{h}^{WG}_{1pc} \rangle$, $\langle \mathbf{e}_{1qs}, \mathbf{h}^{WG}_{2pc} \rangle$, $\langle \mathbf{e}_{2qs}, \mathbf{h}^{WG}_{1pc} \rangle$, and $\langle \mathbf{e}_{2qs}, \mathbf{h}^{WG}_{2pc} \rangle$ must be



solved. These integrals can be solved in closed form for this specific geometry. For example, the coupling between TE rectangular aperture modes and TE Floquet modes is

$$C^{1qs}_{1mn} = \left\langle \mathbf{e}_{1qs}, \mathbf{h}^F_{1mn} \right\rangle = \int_{x=-a_1}^{a_1} \int_{y=-b_1}^{b_1} \mathbf{e}_{1qs} \cdot \mathbf{h}^{F*}_{1mn} dx dy$$

$$= -\frac{1}{2} \frac{1}{k_r^{mn} \sqrt{S_a}} \frac{\sqrt{\epsilon_q \epsilon_s}}{\sqrt{q^2 \frac{b_1}{a_1} + s^2 \frac{a_1}{b_1}}} \times$$

$$\int_{x=-a_1}^{a_1} \int_{y=-b_1}^{b_1} \left\{ k_x^{mn} \frac{q}{a_1} \sin\left[\frac{q\pi x}{2a_1} + \frac{q\pi}{2}\right] \cos\left[\frac{s\pi y}{2b_1} + \frac{s\pi}{2}\right] + \right.$$

$$\left. k_y^{mn} \frac{s}{b_1} \cos\left[\frac{q\pi x}{2a_1} + \frac{q\pi}{2}\right] \sin\left[\frac{s\pi y}{2b_1} + \frac{s\pi}{2}\right] \right\} e^{jxk_x^{mn}} e^{jyk_y^{mn}} dx dy$$

This is solved to yield

$$C^{1qs}_{1mn} = -\frac{\pi}{4} \frac{k_x^{mn} k_y^{mn}}{k_r^{mn} \sqrt{S_a}} \frac{\sqrt{\epsilon_q \epsilon_s}}{\sqrt{q^2 \frac{b_1}{a_1} + s^2 \frac{a_1}{b_1}}} \frac{1}{\left(\frac{q\pi}{2a_1}\right)^2 - \left(k_x^{mn}\right)^2} \frac{1}{\left(\frac{s\pi}{2b_1}\right)^2 - \left(k_y^{mn}\right)^2} \times$$

$$\left\{ \left(\frac{q}{a_1}\right)^2 \left\{ -j\left[1+(-1)^q\right] \sin\left(k_x^{mn} a_1\right) + \left[1-(-1)^q\right] \cos\left(k_x^{mn} a_1\right) \right\} \times \right.$$

$$\left\{ -\left[1+(-1)^s\right] \sin\left(k_y^{mn} b_1\right) - j\left[1-(-1)^s\right] \cos\left(k_y^{mn} b_1\right) \right\} +$$

$$\left(\frac{s}{b_1}\right)^2 \left\{ -\left[1+(-1)^q\right] \sin\left(k_x^{mn} a_1\right) - j\left[1-(-1)^q\right] \cos\left(k_x^{mn} a_1\right) \right\} \times$$

$$\left. \left\{ -j\left[1+(-1)^s\right] \sin\left(k_y^{mn} b_1\right) + \left[1-(-1)^s\right] \cos\left(k_y^{mn} b_1\right) \right\} \right\}$$

The remaining aperture to Floquet-mode coupling integrals are

$$C_{2mn}^{1qs} = \frac{\pi}{4}\frac{1}{k_r^{mn}\sqrt{S_a}}\frac{\sqrt{\epsilon_q\epsilon_s}}{\sqrt{q^2\frac{b_1}{a_1}+s^2\frac{a_1}{b_1}}}\frac{1}{\left(\frac{q\pi}{2a_1}\right)^2-\left(k_x^{mn}\right)^2}\frac{1}{\left(\frac{s\pi}{2b_1}\right)^2-\left(k_y^{mn}\right)^2}\times$$

$$\left\{\left(\frac{qk_y^{mn}}{a_1}\right)^2\left(\left\{-j\left[1+(-1)^q\right]\sin\left(k_x^{mn}a_1\right)+\left[1-(-1)^q\right]\cos\left(k_x^{mn}a_1\right)\right\}\times\right.\right.$$

$$\left\{-\left[1+(-1)^s\right]\sin\left(k_y^{mn}b_1\right)-j\left[1-(-1)^s\right]\cos\left(k_y^{mn}b_1\right)\right\}\Big) -$$

$$\left(\frac{sk_x^{mn}}{b_1}\right)^2\left(\left\{-\left[1+(-1)^q\right]\sin\left(k_x^{mn}a_1\right)-j\left[1-(-1)^q\right]\cos\left(k_x^{mn}a_1\right)\right\}\times\right.$$

$$\left.\left.\left\{-j\left[1+(-1)^s\right]\sin\left(k_y^{mn}b_1\right)+\left[1-(-1)^s\right]\cos\left(k_y^{mn}b_1\right)\right\}\right)\right\}$$

$$C_{1mn}^{2qs} = -\frac{\pi sq}{2a_1b_1}\frac{k_x^{mn}k_y^{mn}}{k_r^{mn}\sqrt{S_a}}\frac{1}{\sqrt{q^2\frac{b_1}{a_1}+s^2\frac{a_1}{b_1}}}\frac{1}{\left(\frac{q\pi}{2a_1}\right)^2-\left(k_x^{mn}\right)^2}\frac{1}{\left(\frac{s\pi}{2b_1}\right)^2-\left(k_y^{mn}\right)^2}\times$$

$$\left\{\left(\left\{-j\left[1+(-1)^q\right]\sin\left(k_x^{mn}a_1\right)+\left[1-(-1)^q\right]\cos\left(k_x^{mn}a_1\right)\right\}\times\right.\right.$$

$$\left\{-\left[1+(-1)^s\right]\sin\left(k_y^{mn}b_1\right)-j\left[1-(-1)^s\right]\cos\left(k_y^{mn}b_1\right)\right\}\Big) -$$

$$\left(\left\{-\left[1+(-1)^q\right]\sin\left(k_x^{mn}a_1\right)-j\left[1-(-1)^q\right]\cos\left(k_x^{mn}a_1\right)\right\}\times\right.$$

$$\left.\left.\left\{-j\left[1+(-1)^s\right]\sin\left(k_y^{mn}b_1\right)+\left[1-(-1)^s\right]\cos\left(k_y^{mn}b_1\right)\right\}\right)\right\}$$

$$C_{2mn}^{2qs} = \frac{\pi sq}{2a_1b_1}\frac{1}{k_r^{mn}\sqrt{S_a}}\frac{1}{\sqrt{q^2\frac{b_1}{a_1}+s^2\frac{a_1}{b_1}}}\frac{1}{\left(\frac{q\pi}{2a_1}\right)^2-\left(k_x^{mn}\right)^2}\frac{1}{\left(\frac{s\pi}{2b_1}\right)^2-\left(k_y^{mn}\right)^2}\times$$

$$\left\{\left(k_y^{mn}\right)^2\left(\left\{-j\left[1+(-1)^q\right]\sin\left(k_x^{mn}a_1\right)+\left[1-(-1)^q\right]\cos\left(k_x^{mn}a_1\right)\right\}\times\right.\right.$$

$$\left\{-\left[1+(-1)^s\right]\sin\left(k_y^{mn}b_1\right)-j\left[1-(-1)^s\right]\cos\left(k_y^{mn}b_1\right)\right\}\Big) -$$

$$\left(k_x^{mn}\right)^2\left(\left\{-\left[1+(-1)^q\right]\sin\left(k_x^{mn}a_1\right)-j\left[1-(-1)^q\right]\cos\left(k_x^{mn}a_1\right)\right\}\times\right.$$

$$\left.\left.\left\{-j\left[1+(-1)^s\right]\sin\left(k_y^{mn}b_1\right)+\left[1-(-1)^s\right]\cos\left(k_y^{mn}b_1\right)\right\}\right)\right\}$$



The coupling between TE rectangular aperture modes and TE rectangular waveguide modes is

$$K_{1pc}^{1qs} = \left\langle \mathbf{e}_{1qs}, \mathbf{h}_{1pc}^{WG}\right\rangle$$

$$= -\frac{1}{\pi^2}\frac{\sqrt{\epsilon_q\epsilon_s}}{\sqrt{q^2\frac{b_1}{a_1}+s^2\frac{a_1}{b_1}}}\frac{\sqrt{\epsilon_p\epsilon_c}}{\sqrt{p^2\frac{b_2}{a_2}+c^2\frac{a_2}{b_2}}}\times$$

$$\left\{\frac{pq}{a_1a_2}\left(\left\{\cos\left[(q-p)\pi/2\right]\frac{\sin\left[(q/a_1-p/a_2)\pi a_1/2\right]}{(q/a_1-p/a_2)}-\right.\right.\right.$$

$$\left.\cos\left[(q+p)\pi/2\right]\frac{\sin\left[(q/a_1+p/a_2)\pi a_1/2\right]}{(q/a_1+p/a_2)}\right\}\times$$

$$\left\{\cos\left[(s-c)\pi/2\right]\frac{\sin\left[(s/b_1-c/b_2)\pi b_1/2\right]}{(s/b_1-c/b_2)}+\right.$$

$$\left.\left.\cos\left[(s+c)\pi/2\right]\frac{\sin\left[(s/b_1+c/b_2)\pi b_1/2\right]}{(s/b_1+c/b_2)}\right\}\right)+$$

$$\frac{cs}{b_1b_2}\left(\left\{\cos\left[(q-p)\pi/2\right]\frac{\sin\left[(q/a_1-p/a_2)\pi a_1/2\right]}{(q/a_1-p/a_2)}+\right.\right.$$

$$\left.\cos\left[(q+p)\pi/2\right]\frac{\sin\left[(q/a_1+p/a_2)\pi a_1/2\right]}{(q/a_1+p/a_2)}\right\}\times$$

$$\left\{\cos\left[(s-c)\pi/2\right]\frac{\sin\left[(s/b_1-c/b_2)\pi b_1/2\right]}{(s/b_1-c/b_2)}-\right.$$

$$\left.\left.\cos\left\{(s+c)\pi/2\right]\frac{\sin\left[(s/b_1+c/b_2)\pi b_1/2\right]}{(s/b_1+c/b_2)}\right\}\right)\right\}$$

The remaining rectangular aperture to rectangular waveguide-mode coupling integrals are

$$K_{2pc}^{1qs} = -\frac{2}{\pi^2}\frac{\sqrt{\epsilon_q\epsilon_s}}{\sqrt{q^2\frac{b_1}{a_1}+s^2\frac{a_1}{b_1}}}\frac{1}{\sqrt{p^2\frac{b_2}{a_2}+c^2\frac{a_2}{b_2}}}\times$$

$$\left\{\frac{qc}{a_1b_2}\left(\left\{\cos[(q-p)\pi/2]\frac{\sin[(q/a_1-p/a_2)\pi a_1/2]}{(q/a_1-p/a_2)}-\right.\right.\right.$$

$$\left.\cos[(q+p)\pi/2]\frac{\sin[(q/a_1+p/a_2)\pi a_1/2]}{(q/a_1+p/a_2)}\right\}\times$$

$$\left\{\cos[(s-c)\pi/2]\frac{\sin[(s/b_1-c/b_2)\pi b_1/2]}{(s/b_1-c/b_2)}+\right.$$

$$\left.\left.\cos[(s+c)\pi/2]\frac{\sin[(s/b_1+c/b_2)\pi b_1/2]}{(s/b_1+c/b_2)}\right\}\right)-$$

$$\frac{sp}{a_2b_1}\left(\left\{\cos[(q-p)\pi/2]\frac{\sin[(q/a_1-p/a_2)\pi a_1/2]}{(q/a_1-p/a_2)}+\right.\right.$$

$$\left.\cos[(q+p)\pi/2]\frac{\sin[(q/a_1+p/a_2)\pi a_1/2]}{(q/a_1+p/a_2)}\right\}\times$$

$$\left\{\cos[(s-c)\pi/2]\frac{\sin[(s/b_1-c/b_2)\pi b_1/2]}{(s/b_1-c/b_2)}-\right.$$

$$\left.\left.\left.\cos[(s+c)\pi/2]\frac{\sin[(s/b_1+c/b_2)\pi b_1/2]}{(s/b_1+c/b_2)}\right\}\right)\right\}$$

$$K_{1pc}^{2qs} = -\frac{2}{\pi^2}\frac{1}{\sqrt{q^2\frac{b_1}{a_1}+s^2\frac{a_1}{b_1}}}\frac{\sqrt{\epsilon_p\epsilon_c}}{\sqrt{p^2\frac{b_2}{a_2}+c^2\frac{a_2}{b_2}}}\times$$

$$\left\{\frac{sp}{b_1a_2}\left(\left\{\cos[(q-p)\pi/2]\frac{\sin[(q/a_1-p/a_2)\pi a_1/2]}{(q/a_1-p/a_2)}-\right.\right.\right.$$

$$\left.\cos[(q+p)\pi/2]\frac{\sin[(q/a_1+p/a_2)\pi a_1/2]}{(q/a_1+p/a_2)}\right\}\times$$

$$\left\{\cos[(s-c)\pi/2]\frac{\sin[(s/b_1-c/b_2)\pi b_1/2]}{(s/b_1-c/b_2)}+\right.$$

$$\left.\left.\cos[(s+c)\pi/2]\frac{\sin[(s/b_1+c/b_2)\pi b_1/2]}{(s/b_1+c/b_2)}\right\}\right)-$$



$$\frac{qc}{a_1b_2}\left(\left\{\cos[(q-p)\pi/2]\frac{\sin[(q/a_1-p/a_2)\pi a_1/2]}{(q/a_1-p/a_2)}+\right.\right.$$

$$\left.\cos[(q+p)\pi/2]\frac{\sin[(q/a_1+p/a_2)\pi a_1/2]}{(q/a_1+p/a_2)}\right\}\times$$

$$\left\{\cos[(s-c)\pi/2]\frac{\sin[(s/b_1-c/b_2)\pi b_1/2]}{(s/b_1-c/b_2)}-\right.$$

$$\left.\left.\cos[(s+c)\pi/2]\frac{\sin[(s/b_1+c/b_2)\pi b_1/2]}{(s/b_1+c/b_2)}\right\}\right)\right\}$$

$$K_{2pc}^{2qs} = -\frac{4}{\pi^2}\frac{1}{\sqrt{q^2\frac{b_1}{a_1}+s^2\frac{a_1}{b_1}}}\frac{1}{\sqrt{p^2\frac{b_2}{a_2}+c^2\frac{a_2}{b_2}}}\times$$

$$\left\{\frac{sc}{b_1b_2}\left(\left\{\cos[(q-p)\pi/2]\frac{\sin[(q/a_1-p/a_2)\pi a_1/2]}{(q/a_1-p/a_2)}-\right.\right.\right.$$

$$\left.\cos[(q+p)\pi/2]\frac{\sin[(q/a_1+p/a_2)\pi a_1/2]}{(q/a_1+p/a_2)}\right\}\times$$

$$\left\{\cos[(s-c)\pi/2]\frac{\sin[(s/b_1-c/b_2)\pi b_1/2]}{(s/b_1-c/b_2)}+\right.$$

$$\left.\left.\cos[(s+c)\pi/2]\frac{\sin[(s/b_1+c/b_2)\pi b_1/2]}{(s/b_1+c/b_2)}\right\}\right)+$$

$$\frac{qp}{a_1a_2}\left(\left\{\cos[(q-p)\pi/2]\frac{\sin[(q/a_1-p/a_2)\pi a_1/2]}{(q/a_1-p/a_2)}+\right.\right.$$

$$\left.\cos[(q+p)\pi/2]\frac{\sin[(q/a_1+p/a_2)\pi a_1/2]}{(q/a_1+p/a_2)}\right\}\times$$

$$\left\{\cos[(s-c)\pi/2]\frac{\sin[(s/b_1-c/b_2)\pi b_1/2]}{(s/b_1-c/b_2)}-\right.$$

$$\left.\left.\cos[(s+c)\pi/2]\frac{\sin[(s/b_1+c/b_2)\pi b_1/2]}{(s/b_1+c/b_2)}\right\}\right)\right\}$$

CHAPTER SIX

# Frequency Selective Surface Materials and Fabrication

GREGORY S. HICKEY, Jet Propulsion Laboratory, California Institute of Technology, Pasadena, California

The material properties and fabrication processes have a direct effect on the electrical performance of frequency selective surfaces (FSS) and grid arrays. A typical FSS is composed of an electrical grid array of a conductive material supported on a dielectric structure. The dielectric structure may be a polymer film, a homogeneous ceramic, or a heterogeneous fiber-reinforced polymeric composite. Because there may be more than one material composing the supporting structure, their individual electrical properties become important for FSS performance.

The electrical performance of materials at microwave frequencies has been a subject of interest and characterization for a long time. This interest arises for two primary reasons. The first is the electrical performance of materials in practical applications. The second is that the measurement techniques at microwave frequencies have evolved to allow the study of the molecular structure of materials. The physical and electrical properties, such as complex relative permeability and permittivity or dielectric constant, are intrinsic properties of the material and are related to their molecular structure. Many extrinsic properties are also affected by processing and affect electrical performance. Examples are density and porosity, molecular weight of polymeric materials, and the interaction of heterogeneous materials of composite structures.

*Frequency Selective Surface and Grid Array*, Edited by T. K. Wu
ISBN 0-471-31189-8 © 1995 John Wiley & Sons, Inc.

## 6.1 DIELECTRIC PROPERTIES OF MATERIALS

The electrical properties of a material can be expressed in terms of its complex relative permeability $\mu = \mu' - j\mu''$ with a loss tangent $\tan \delta_\mu = \mu''/\mu'$ and complex permittivity $\epsilon = \epsilon' - j\epsilon''$ with a loss tangent $\tan \delta_\epsilon = \epsilon''/\epsilon'$. The two properties are a measure of the polarization that a material undergoes in an applied magnetic or electrical field. The permeability depends on the magnetic field, and the permittivity depends on the electrical field. Both permeability and permittivity vary with frequency to give responses in one of two types. This is illustrated in Figure 6.1. The first is the Debye relaxation, which is caused by the frequency being of a high enough value that the

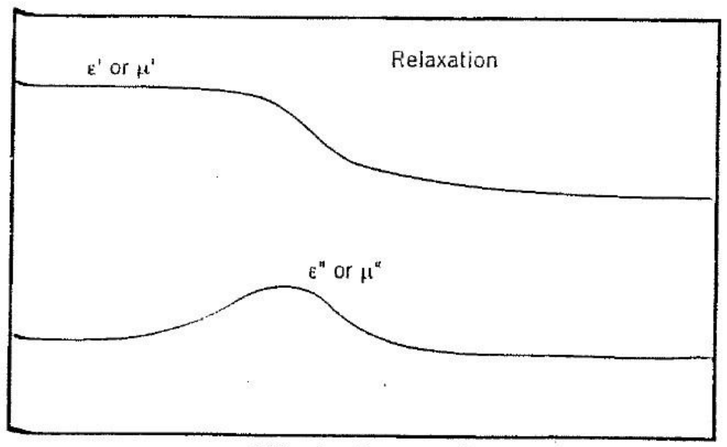


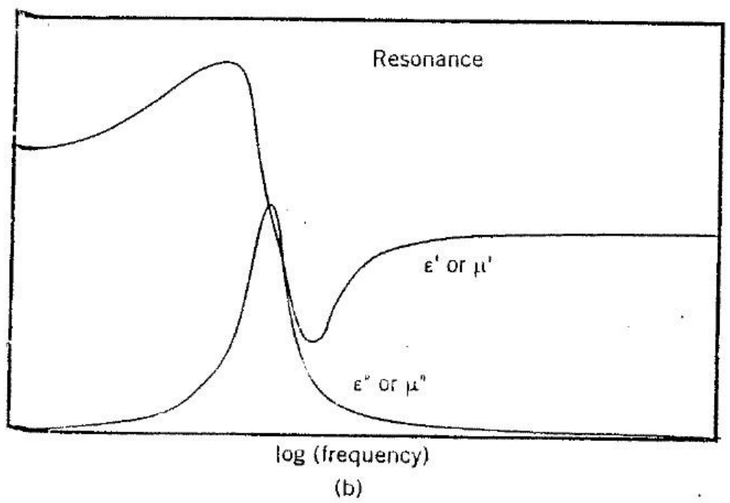


**FIGURE 6.1** Relaxation (a) and resonance (b) response of a dielectric material.



induced polarizations in the material cannot establish themselves before the frequency cycle is reversed. In this case the relative permittivity and permeability change slowly over a frequency range with an associated adsorption band centered on the frequency $\frac{1}{2}\pi\tau$. These are broad relaxation bands with a maximum peak at $\tan \delta$ for both permeability and permittivity. The second type of dispersion is associated with quantized transitions $\Delta W = h\nu_r$ from one atomic energy level to another in the atom or nucleus. When the applied frequency equals $\nu_r$, resonance occurs and there is a sharp adsorption band. This type of quantized material response for the material is of interest in electron resonance spectroscopy.

For nonferromagnetic materials, the relative permeability is near unity. Therefore it is the material's permittivity in electrical fields that becomes important. The relative permittivity, or dielectric constant, is associated with polarizations consisting of relative displacement of positive and negative charges within an atom or molecule. The loss mechanism is considered to be associated with the relaxation process. For this reason the dielectric constant, $\epsilon$, and the loss tangent are the two most important properties in describing the electrical response of materials for FSS and grid arrays. The dielectric constant and loss tangent for most materials of interest will have a temperature dependence. This results from the internal electronic structure of the atom or molecule. A spacecraft antenna application may have a temperature environmental range from $-100°C$ to $+100°C$; an aircraft application will have a smaller temperature range, from $-40°C$ to $60°C$. At the lower temperature ranges, the dielectric constant remains constant and the loss tangent approaches a minimum. At higher temperature ranges, there is a small increase in the dielectric constant, associated with a significant increase in the loss tangent. The amount of variation depends on the specific material system. An example is presented in the following section.

## 6.2 FSS MATERIALS AND FABRICATION

Frequency selective surface arrays are typically supported on are fiber-reinforced dielectric composite structure. For many applications this is a multiple-layer composite facesheet, but in most cases it is a composite honeycomb structure. A typical such structure is shown in Figure 6.2, it consists of two thin dielectric fiber-reinforced polymeric composite facesheets attached to a structural core. The facesheets are typically bonded to the core by an adhesive, but the facesheets may be cocured with the core to provides a structural bond. The FSS array would be on one or more of the facesheet surfaces. In multiple FSS surface designs, the spacing of the surfaces becomes important. It is usually desirable to design the structure with a low electrical dielectric constant and with a low electrical loss for the frequencies of interest. Some designs require the structure to have a finite dielectric

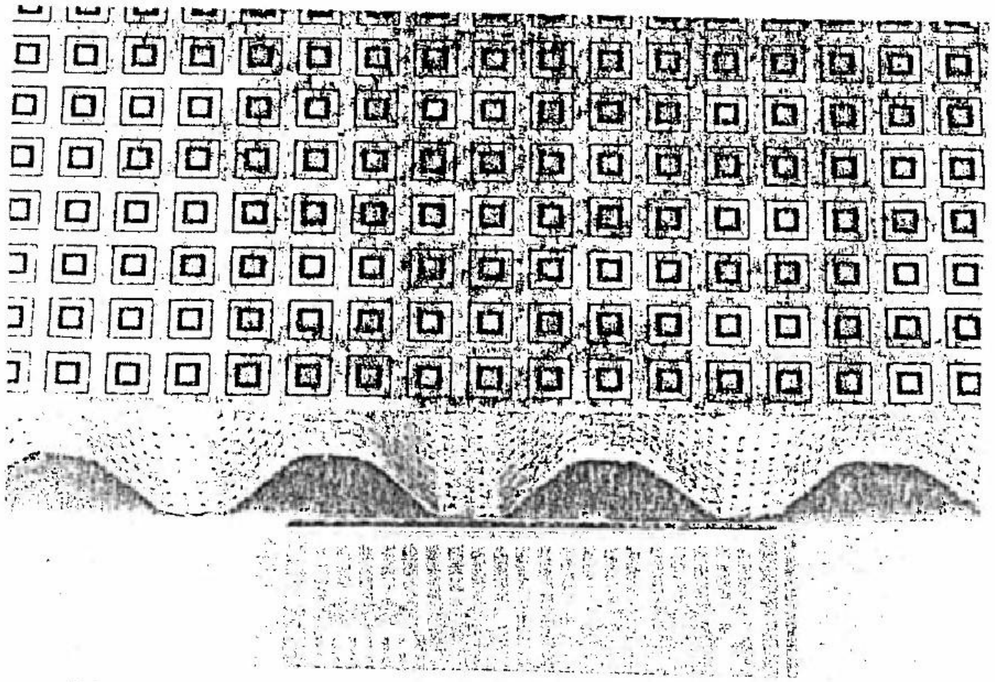

FIGURE 6.2 Typical composite structure with frequency selective surface.

constant of moderate value, usually from 8 to 13. An example is the four-frequency design on a single screen described in Chapter 4.

There have been many good references on the mechanical design and fabrication of composite structures in recent years, as the technology has emerged to a broad base of applications. Jones [1] and Tsai [2] provide a good treatise on the mechanical properties of composite and honeycomb structures, and Schwartz [3] provides an overview of the current state of the art for composite fabrication processes. In this section the electrical properties of the materials used in FSS arrays and fabrication processes specific to FSS structures are reviewed.

Frequency selective surfaces and grid arrays consist of conductive grid arrays, usually thin copper film on a dielectric film or structure. The electrical design and performance of the FSS are directly affected by the electrical characteristics of the supporting film or structure. If the FSS is supported simply by a film, the electrical design is straightforward, using the known electrical properties of the materials. If the FSS or grid array is supported by a structure, the electrical design must include the effective electrical properties of the constitutive materials. For a fiber-reinforced composite, this would include the fiber, polymeric resin, adhesives, and core. The electrical design must include any air gaps or spaces that may be present either as open cells in a foam or composite core or as porosity in a polymeric composite. For most applications of technological interest, the FSS is fabricated on a



dielectric film that is supported by a structure. The electrical properties of each constituent are reviewed, first separately and then as a structure.

Generally, the FSS screen is fabricated by the thick-film chemical etching of a copper-coated thin film using standard circuit board processes. A typical film that might be used is Kapton polyimide film from DuPont. Mylar has been used in the past, but it has mostly been replaced by Kapton. Kapton is a well-characterized and stable film that has found broad applications in flexible circuits. It has excellent thermal, dimensional, and radiation stability and is readily available as films from 0.5 to 5 mils thick, either plain or metallized with copper. Its dielectric constant is between 3.23 and 3.4 in the gigahertz frequency range, with a dissipation factor about 0.008, and its temperature application range is −269°C to 400°C.

It is possible to employ the same chemical-etching techniques directly with a metallized composite facesheet. For flat surfaces there are several suppliers of metallized glass–epoxy sheet material, and the FSS can be directly fabricated on the material. For designs where the surface must have a finite dielectric constant of moderate value, the FSS is fabricated onto a prepared material of known dielectric property. An example of such a material is RT Duroid from the Rogers Corporation. For a curved FSS design, it is usually not practical to metallize the structure, so the FSS array is fabricated on a Kapton screen.

As shown in Figure 6.2, the composite facesheets comprise a structural fiber that is supported by the polymeric resin. The choice of the fiber and resin system is determined by the electrical, mechanical, and environmental requirements that FSS will see. For most applications the materials are selected to minimize the electrical loss and to optimize mechanical strength and stiffness, but for some specific spacecraft applications the environmental requirements determine the selection and choice of materials.

For a well-designed and fabricated composite, the fibers and resin are well distributed over the surface area. Most structural composites have 50 to 60% fiber content by volume, with the balance being the polymeric resin. For very thin composite facesheets, there may also be some degree of porosity. The composite facesheets are fabricated as a laminate from several layers of fiber and resin lamina. To maintain quality control over the fiber and resin distribution, the fiber and resin lamina are obtained as manufactured prepreg. The prepreg is obtained with a fixed fiber and resin content, with the resin in a partially cured state, in one of two primary forms, depending on fiber placement. The first is a unidirectional tape, available from 6 to 12 in widths. In this form all the fibers are aligned parallel to each other. The other form is a prewoven cloth impregnated with resin. In this form there are usually an equal number of fibers oriented parallel and perpendicular to each other. Dozens of different fabric weaves are available to give a broad selection of fiber areal densities and mechanical properties. Prepreg fabrics may be from 30 to 60 in wide. The weaves are typically fine enough to provide a balanced distribution of the fibers, so there is no anisotropy of the electrical properties for the frequencies of interest.

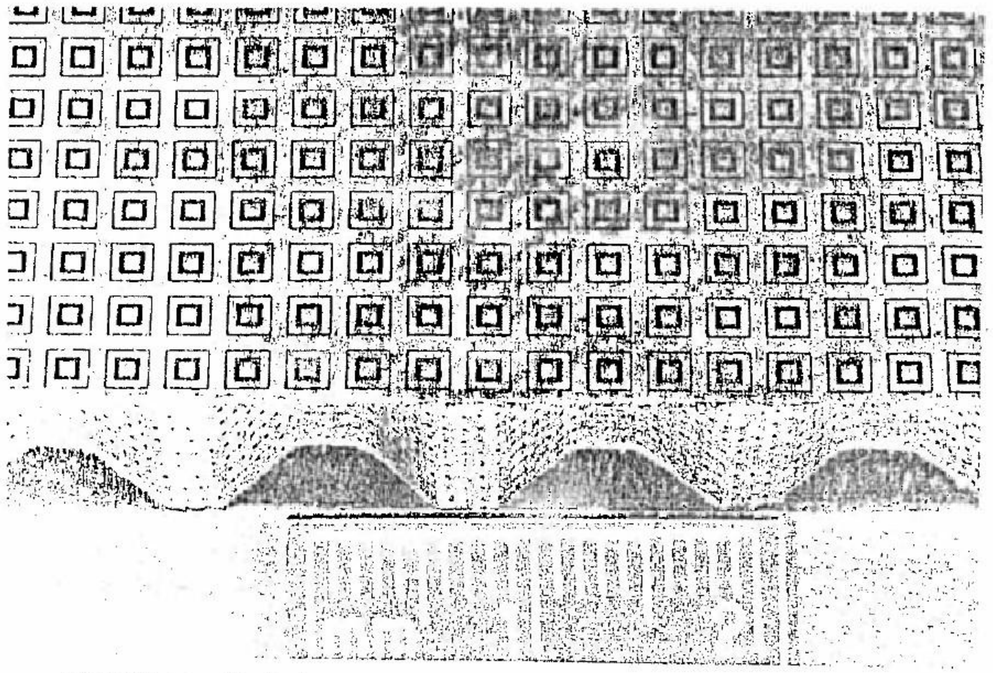

**FIGURE 6.2** Typical composite structure with frequency selective surface.

constant of moderate value, usually from 8 to 13. An example is the four-frequency design on a single screen described in Chapter 4.

There have been many good references on the mechanical design and fabrication of composite structures in recent years, as the technology has emerged to a broad base of applications. Jones [1] and Tsai [2] provide a good treatise on the mechanical properties of composite and honeycomb structures, and Schwartz [3] provides an overview of the current state of the art for composite fabrication processes. In this section the electrical properties of the materials used in FSS arrays and fabrication processes specific to FSS structures are reviewed.

Frequency selective surfaces and grid arrays consist of conductive grid arrays, usually thin copper film on a dielectric film or structure. The electrical design and performance of the FSS are directly affected by the electrical characteristics of the supporting film or structure. If the FSS is supported simply by a film, the electrical design is straightforward, using the known electrical properties of the materials. If the FSS or grid array is supported by a structure, the electrical design must include the effective electrical properties of the constitutive materials. For a fiber-reinforced composite, this would include the fiber, polymeric resin, adhesives, and core. The electrical design must include any air gaps or spaces that may be present either as open cells in a foam or composite core or as porosity in a polymeric composite. For most applications of technological interest, the FSS is fabricated on a



dielectric film that is supported by a structure. The electrical properties of each constituent are reviewed, first separately and then as a structure.

Generally, the FSS screen is fabricated by the thick-film chemical etching of a copper-coated thin film using standard circuit board processes. A typical film that might be used is Kapton polyimide film from DuPont. Mylar has been used in the past, but it has mostly been replaced by Kapton. Kapton is a well-characterized and stable film that has found broad applications in flexible circuits. It has excellent thermal, dimensional, and radiation stability and is readily available as films from 0.5 to 5 mils thick, either plain or metallized with copper. Its dielectric constant is between 3.23 and 3.4 in the gigahertz frequency range, with a dissipation factor about 0.008, and its temperature application range is $-269°C$ to $400°C$.

It is possible to employ the same chemical-etching techniques directly with a metallized composite facesheet. For flat surfaces there are several suppliers of metallized glass–epoxy sheet material, and the FSS can be directly fabricated on the material. For designs where the surface must have a finite dielectric constant of moderate value, the FSS is fabricated onto a prepared material of known dielectric property. An example of such a material is RT Duroid from the Rogers Corporation. For a curved FSS design, it is usually not practical to metallize the structure, so the FSS array is fabricated on a Kapton screen.

As shown in Figure 6.2, the composite facesheets comprise a structural fiber that is supported by the polymeric resin. The choice of the fiber and resin system is determined by the electrical, mechanical, and environmental requirements that FSS will see. For most applications the materials are selected to minimize the electrical loss and to optimize mechanical strength and stiffness, but for some specific spacecraft applications the environmental requirements determine the selection and choice of materials.

For a well-designed and fabricated composite, the fibers and resin are well distributed over the surface area. Most structural composites have 50 to 60% fiber content by volume, with the balance being the polymeric resin. For very thin composite facesheets, there may also be some degree of porosity. The composite facesheets are fabricated as a laminate from several layers of fiber and resin lamina. To maintain quality control over the fiber and resin distribution, the fiber and resin lamina are obtained as manufactured prepreg. The prepreg is obtained with a fixed fiber and resin content, with the resin in a partially cured state, in one of two primary forms, depending on fiber placement. The first is a unidirectional tape, available from 6 to 12 in widths. In this form all the fibers are aligned parallel to each other. The other form is a prewoven cloth impregnated with resin. In this form there are usually an equal number of fibers oriented parallel and perpendicular to each other. Dozens of different fabric weaves are available to give a broad selection of fiber areal densities and mechanical properties. Prepreg fabrics may be from 30 to 60 in wide. The weaves are typically fine enough to provide a balanced distribution of the fibers, so there is no anisotropy of the electrical properties for the frequencies of interest.

The prepreg is oriented in several layers to provide the desired structural properties. Prepreg unidirectional tape is usually 3 to 4 mils thick, prepreg fabrics 5 to 8 mils thick. Thinner weaves and areal densities to produce 1–2 mil thicknesses are available as specialty products. The prepreg lamina are cured thermally to the desired structural shape either in an autoclave at 50 to 200 psi pressure or, for thin laminates, under a vacuum bag in an oven at 15 psi pressure. Typical facesheets for FSS applications are 10 to 20 mils thick, to minimize the amount of structural material to minimize electrical losses.

Electrical properties of the composite facesheets are determined by the constitutive electrical properties of the fiber and resin. The fiber and resin each have distinct electrical properties, but when they are fabricated as a composite the resulting material has homogeneous electrical properties. Because of the complex microscopic behavior for the constitutive materials, there is no direct analytical approach to determine the dielectric constant or loss tangent. An approximate technique to estimate the dielectric constant is to use a rule-of-mixtures approach:

$$\epsilon_{\text{composite}} = V_f \epsilon_f + V_r \epsilon_r + V_p \epsilon_p,$$

where $V_f$ is the percent fiber by volume, $V_r$ is the percent resin by volume, $V_p$ is the percent porosity by volume, and $\epsilon_f$, $\epsilon_r$, and $\epsilon_p$ are the dielectric constants for the fibers, resin, and porosity, respectively. The porosity is included in the determination of the electrical properties because even a small amount may affect the resonant frequency for FSS arrays. The porosity is usually air or vacuum and has a dielectric constant of unity. There is no direct approach to estimate the loss factor for a composite material. For accurate modeling, both the dielectric constant and the loss tangent are best determined by measurement as described in Chapter 1.

The primary selection requirements in the choice of material system are the radio-frequency (RF) compatibility with low dielectric loss, survivability in the application environment, and the ability to manufacture a low-thermal-expansion, dimensionally stable composite structure. The importance of these requirements depends on the application of the FSS. For ground-based applications the most significant requirement is the material's electrical performance. For an aircraft radome application the environmental stability and dimensional stability are important, since the radome may experience a thermal environment from −40°C to +60°C in air. For a space application of an FSS, the thermal environment may range from −100°C to +100°C for a satellite in an earth-based orbit, to −130°C to +175°C for an interplanetary spacecraft such as NASA's Cassini interplanetary probe to Saturn. For earth-based geosynchronous and low-earth-orbit satellites, the temperature range varies from time period in and out of the view of the sun. Within view of the sun, the FSS will approach thermal equilibrium, though there may be significant thermal gradients based on the angle of the field of view. When the satellite FSS is out of view of the sun, the FSS loses heat to



the surrounding environment. Since the structures are made of dielectric materials, they generally have low thermal heat capacity and thermal conductivity. For interplanetary spacecraft the thermal environment that the FSS sees strongly depends on the spacecraft trajectory. For example, the Cassini spacecraft has a planetary trajectory where it will undergo a Venus fly-by to gather momentum to reduce the transit time to Saturn. Near Venus, the FSS on the Cassini will have a high solar thermal input, but near Saturn it will have only a fraction of the solar thermal input. Thermal control may be assisted by thermal control coatings, but currently available coatings have measurable dielectric loss and affect FSS array performance.

The fibers provide the primary structural properties for the FSS in a composite structure. Dielectric fibers currently in widespread use in composites are glass, quartz, Kevlar 49, and Spectra 1000. Glass and fused quartz are inorganic fibers, whereas Kevlar 49 is an organic aramid fiber and Spectra 1000 is an oriented high-density linear polyethylene fiber. Glass fibers are available as E glass or S glass in developmental form as hollow fibers, with similar mechanical properties and an improvement in their electrical properties. Table 6.1 summarizes the electrical properties of the fibers.

Glass fibers are the most commonly available fibers, and hence the least expensive. Fused quartz has the lowest dielectric constant, but is the most expensive. Hollow glass fibers have up to 30% hollow volume and are attractive for weight-sensitive spacecraft applications. The Spectra fiber has the lowest density and a good combination of electrical and mechanical properties, but it is thermally unstable at temperatures above 130°C. This would seriously limit its application for many uses. The mechanical properties of the fibers determine their use in dimensionally stable applications. Table 6.2 gives the fiber longitudinal coefficient thermal expansion (CTE) properties and the resulting thermal expansion for a quasi-isotropic composite. The CTE of quasi-isotropic composites presented is an analytical result that assumes a 60% fiber volume with polymer matrix of a typical epoxy. The results are based on using micromechanical modeling of composite laminates

**TABLE 6.1. Electrical Properties at 20°C and 10 GHz of Common Dielectric Fibers Alone and as Composites (assumes 40% epoxy resin)**

| | Fiber | | Composite | |
|---|---|---|---|---|
| Fiber | Dielectric Constant | Loss Tangent | Dielectric Constant | Loss Tangent |
| S-2 glass | 5.21 | .007 | 3.90 | .014 |
| E glass | 6.13 | .004 | 4.70 | .015 |
| Fused quartz | 3.78 | .0001 | 3.52 | .017 |
| Kevlar 49 | 3.55 | .010 | 3.45 | .015 |
| Spectral 1000 | 2.30 | .0004 | 2.42 | .005 |
| Hollow S-2 glass | 3.20 | .005 | 3.20 | .012 |
| Hollow E glass | 3.95 | .004 | 3.70 | 0.014 |

TABLE 6.2. Mechanical Properties of Composite Laminates Using Dielectric Fibers

| | Kevlar 49 | E Glass | Quartz |
|---|---|---|---|
| Fiber CTE, longitudinal ($\times 10^{-6}$ m/m°C) | −1.1 | 1.55 | 0.80 |
| Fiber CTE, transverse ($\times 10^{-6}$ m/m°C) | 28.0 | 1.55 | 0.80 |
| Resin CTE, bulk ($\times 10^{-6}$ m/m°C) | 55.0 | 55.0 | 55.0 |
| Quasi-isotropic composite CTE | 0.7 | 10.6 | 5.0 |

with the method of Chamis [4]. As can be seen from Tables 6.1 and 6.2, even though the quartz fibers have better electrical properties than other fibers, they cannot produce the most dimensionally stable composite laminate. For this reason Kevlar is used on many spacecraft FSS that require dimensional stability due to thermal gradients on the structure. This becomes even more important as the application frequency increases and the physical sizes of the FSS elements and their tolerances decrease.

Next to the fiber, the selection of the polymeric resin has the most significant effect on the electrical and mechanical performances of the FSS. The primary consideration in selecting a resin system is its electrical properties and its environmental stability. Many commercially available structural resins are used in composite applications. Hundreds of variations are based on blending and additives of resins to modify their mechanical properties. Fortunately, the electrical properties of structural polymeric resins when grouped as a class do not vary much within the grouping. The four primary classes of resins used in radomes and antennas are epoxies, polyimides, bismaleimides, and cyanate esters (also known as polycyanates). Polyester resins have found use in some nonstructural applications. The most commonly used resin is epoxy, but other resin systems have found applications based on their mechanical or thermal properties. In general, polymeric systems have smaller dielectric constants and loss tangents than do fibers, with variations due to the amount of cross-linking and heteroatoms in the polymer.

When thermal stability is a primary consideration, the most important physical property to compare for thermoset polymers is their glass transition temperature, $T_g$. Physically, above the $T_g$ the polymer softens, and its modulus decreases several orders in magnitude while its thermal expansion increases significantly. For most thermosets, $T_g$ is either at or near the polymer cure temperature. The physical properties of the resin remain constant usually until 30°C below $T_g$. Table 6.3 gives representative physical and electrical properties for polymer resins for each of the four classes. All data are from manufacturer's datasheets. The estimated dielectric constant



TABLE 6.3. Estimated Physical and Electrical Properties of Selected Resins

| Polymer | $T_g$ (°C) | $\epsilon_{polymer}$ | Loss Tangent | $\epsilon_{composite}$ |
|---|---|---|---|---|
| Hexcel F161 epoxy | 170 | 3.03 | 0.010 | 3.42 |
| YLA RS-3 cyanate-ester | 260 | 2.80 | 0.001 | 3.33 |
| Langley NR-150 polyimide | 310 | 3.11 | 0.005 | 3.48 |
| Hexcel F-652 bismaleimide | 315 | 3.05 | 0.006 | 3.45 |

for the composite is based on the rule-of-mixture approach, assuming 60% Kevlar 49 fibers and no porosity.

As can be seen from Table 6.3, the cyanate ester has the best mix of electrical properties and temperature stability. The cyanate ester is processed similar to epoxy thermosets and is now available from several sources. Figure 6.3 shows the cyanate-ester electrical properties as a function of frequency and temperature. The cyanate ester has a very low loss factor, and its dielectric constant is stable over a wide temperature and frequency range. It also has excellent environmental stability, as shown in Figures 6.4 and 6.5. For geosynchronous and especially low-earth-orbit satellites, a source of environmental degradation is from solar radiation captured in the earth's gravitational field. A typical one-year radiation accumulation for a spacecraft in low earth orbit is 1–5 Mrad electron equivalent radiation, with variations due to altitude and inclination. The cyanate ester [5] shows no degradation at 10-Mrad and only minimal change at 1000 Mrad. A typical epoxy has a radiation threshold of 10 Mrad before showing significant change in mechanical properties. It is expected that the electrical properties will be altered at similar radiation exposures levels and that changes in the mechanical properties occur.

The composite facesheets or FSS grid arrays on Kapton film are bonded onto the core with adhesives. Most structural adhesives available are epoxy based, but acrylic, acetate, and other types of adhesives are also used. There are two criteria for the selection of adhesives for FSS applications. The first is that the adhesive should have a low electrical loss and a stable dielectric constant. The second is that the adhesive should have good mechanical properties at the maximum and minimum temperature extremes. The adhesives should preferably be unfilled, because most of the fillers that are added to improve mechanical strength have high electrical loss. For bonding the facesheets onto the core, either film or paste adhesive should be used. Film adhesives are available in 1–3 mil cured thicknesses. The amount of adhesive should be minimized to reduce their effect on the electrical design. If there is

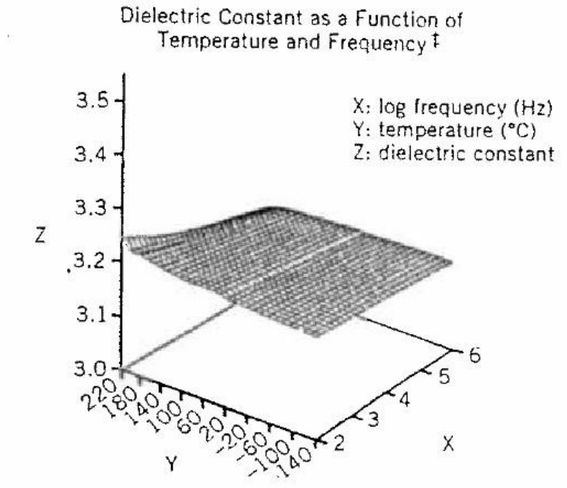


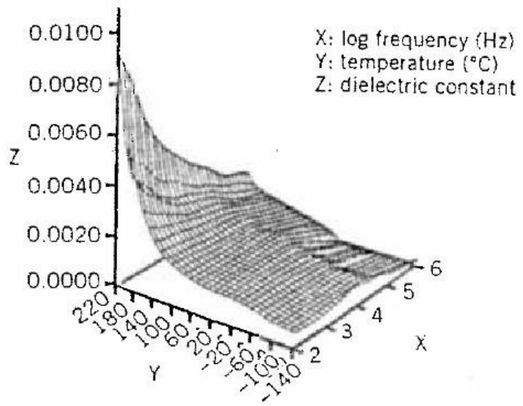


FIGURE 6.3 Electrical properties of a cyanate-ester polymeric resin. (Data courtesy Dow Chemical.)

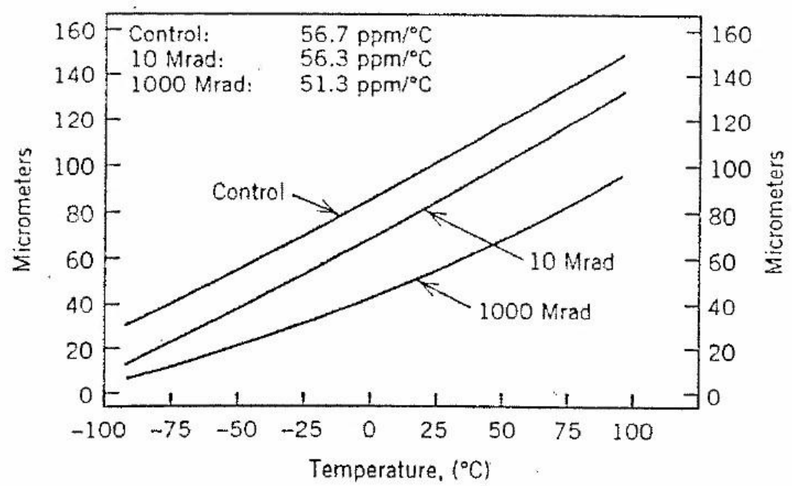




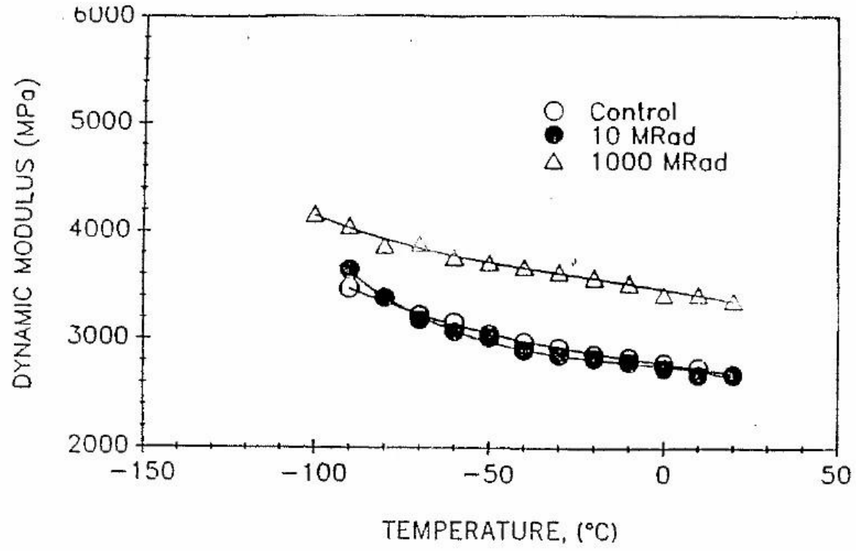


FIGURE 6.5 Mechanical stability of a cyanate-ester polymer resin in a space environment.

a significant amount of adhesive, it should be included as an element in the electrical design. Thick bond lines can act as discontinuities in the electrical performance and at high frequencies they can become critical to the performance. Film adhesives have an advantage over past adhesives in that they can more easily be incorporated into the electrical design because they can be treated as isotropic materials of known thickness and electrical properties. They bond well to both honeycomb and foam cores. Paste adhesives have the advantage that the amount of mass for the adhesive can be reduced when a honeycomb core is used. This is accomplished by applying the paste adhesive onto the honeycomb cell edges with a brush or roller. However, their nonuniform application may complicate the electrical design.

Two types of cores are generally used in the fabrication of FSS dielectric structures: honeycomb composite and polymeric foam. The two most common dielectric honeycomb cores are Nomex- and Kevlar-based cores. Both are aramid-based materials. Nomex is made from an aramid paper, and Kevlar from aramid fibers. They are held together mechanically by phenolic, epoxy, or polyimide resins. S-glass and quartz fiber based honeycomb cores are also available. Of the three resin types, the polyimide-based cores have the best electrical properties. Both perform similarly electrically; but Kevlar has superior mechanical properties.

A third aramid-based honeycomb core, Korex from DuPont, has recently been introduced. Korex has better mechanical properties than Nomex, and its core has a dielectric constant between 1.06 and 1.09, depending on polarization. Both Nomex and Korex can be shaped over curved surfaces and

easily machined. The Kevlar core is stiffer and is difficult to conform over curved surfaces. Special machining techniques must also be used. Honeycomb cores typically have better mechanical properties per weight of material than foam cores, but they are more expensive.

Many available foam cores have good dielectric properties and mechanical integrity, from polyurethane- to polymethacrylimide-based foams. Foams are isotropic in mechanical and electrical properties, which are highly dependent on the density. Typical polyurethane foams have a dielectric constant at 10 GHz of 1.12 with a loss tangent of 0.002. Polymethacrylimide foams have a dielectric constant of 1.06 with a loss tangent of 0.0008 at 10 GHz and a dielectric constant of 1.11 with a loss of 0.0034 at 26 GHz. Most foams are easily machinable and can have either composite facesheets or FSS grid arrays on Kapton film grids bonded onto the surfaces.

For ground-based, aircraft, and shipboard applications, moisture absorption by the core can significantly affect the electrical performance of the FSS. Foam cores may absorb up to 5% or more by weight moisture. Epoxy-based honeycomb cores may adsorb up to 1% by weight moisture. Glass-polyimide or quartz-polyimide honeycomb cores have the least moisture absorption and are recommended for applications where moisture absorption is considered a problem.

Forming the core materials must be considered in the electrical design. When two FSS surfaces are supported between two facesheets of different geometries, the interaction of the core must be taken into account. If an isotropic foam core is used, the varying thicknesses with their associated electrical losses must be considered. If a honeycomb core is used, how it is formed is an important consideration. Nomex cores can be heat-formed over curved surfaces so that the cell walls can be made normal to the FSS grid array surfaces. If the honeycomb core is not heat-formed but is machined out of a large block of material, the cell walls are not likely to be normal to the FSS surfaces. In this case, the apparent loss of transmission through the honeycomb cell walls must be taken into account. When the cell walls are normal to the surface, it is usually a good assumption that the honeycomb has minimal electrical interaction, and can be assumed to have a dielectric constant of unity with no loss. This is a good assumption at lower frequencies because in a typical honeycomb core the cell walls only constitute 3–5% of the areal volume. This assumption fails at higher frequencies when the characteristic dimension of the FSS grids is similar to the core wall thickness, usually 1–3 mils.

## 6.3 FABRICATION OF FSS GRID ARRAYS AND STRUCTURES

The fabrication process for the grid elements on the curved surface of the FSS is a critical technology. The NASA *Voyager* X- and S-band FSS showed that the grid elements were distorted during manufacture. Even with grid-



element distortion, the *Voyager* FSS performed within specification. The emergence of three- and four-frequency FSS at higher frequencies requires more attention to grid dimensional tolerance and registration alignment between layers. Fabrication is an involved process, covering art generation and etching of the FSS grid array, composite structure fabrication, integration of the grid surfaces, alignment and bonding, and RF testing. The entire process may take several months to complete. A block diagram of typical processes involved is shown in Figure 6.6. The exact processes involved depend on the size and complexity of the FSS. The art generation and etching processes have been well-developed from the circuit board industry.

The most difficult process is the fabrication and integration of the FSS grid elements with the dielectric structure surface. Three primary techniques for FSS grid fabrication are used on a curved surface. The first is to form the grid elements on a single flat Kapton sheet and heat-form the surface to a curved geometry. This technique was used on the *Voyager* spacecraft. The second technique uses multiple flat strips of grid elements on Kapton

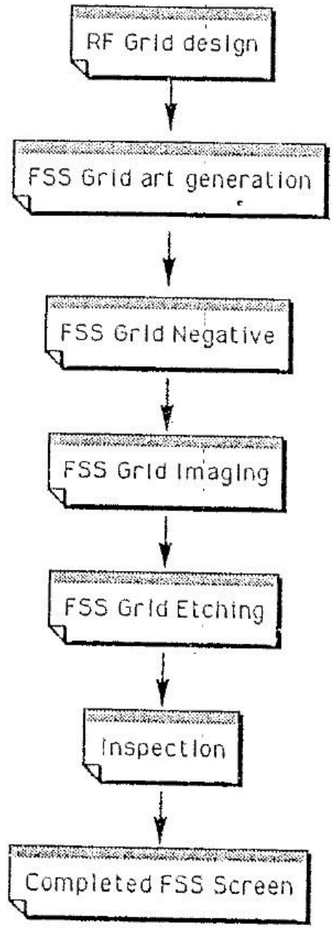


FIGURE 6.6 FSS grid fabrication process.

precisely placed on the curved surface. This technology has been used on ground-based planar array antennas, commercial satellites such as *Intelsat*, and scientific interplanetary spacecraft such as NASA's Cassini mission. The third technique is to image the grid elements directly on the curved surface by as photolithography process. This can be accomplished either by fabricating a mask of the grid elements covering the complete surface or by using a laser to directly image each grid element and to image the periodic grid array across the surface in a stepwise manner. This last technique is still in the developmental stage and has only been demonstrated commercially for simple grid-element patterns over small surfaces of low curvature.

The most common technique is to use the grid-element-strip approach for large FSSs. The element strips must be carefully aligned with one another. Since it is difficult to produce a precise overlay of grids, it is better to design alignment points on the art work and use them for alignment. The integration of an FSS grid array surface into a composite structure is illustrated in Figure 6.7. It shows a multiple-surface FSS structure that has a three-frequency surface and an additional Ka surface. This FSS design was discussed in Chapter 4. The two FSS surfaces are formed independently of each

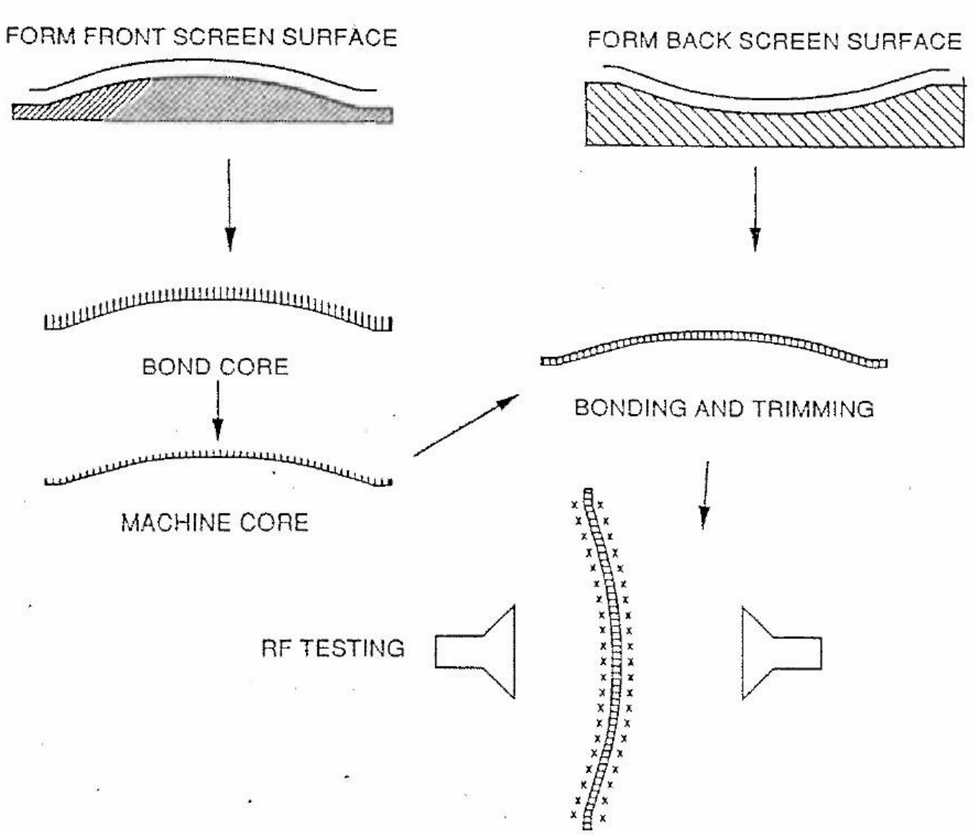


FIGURE 6.7 Multiple-screen FSS fabrication process.



other. The grid elements are laid down on tooling specific for the geometry of each surface in the stripline approach already described. This process is time consuming due to the care and attention needed to maintain registration alignment. The dielectric prepreg is laid up over the grid array and cocured with the composite facesheets. The resin from the polymeric prepreg provide the adhesive bond. For this approach, use of a low-flow resin will not distort the original grid-element alignment. The core is then heat-formed, bonded onto one of the two surfaces, and machined to match the geometry of the other FSS surface. The other FSS surface is then bonded to the machined core surface with the grid array. The original tooling is used throughout this process to provide the proper dimensional surfaces and to maintain alignments. After trimming, the FSS is available for RF testing to validate its performance. Close attention to detail and alignment is very important for a fully functional and low-loss FSS. Registration accuracy is very important for FSS applications in which the grid layers are in close proximity. Precise alignment fixtures must be utilized.

Special consideration must be given to developing FSS for spacecraft. These considerations involve structural, environmental, and contamination requirements that are general to spacecraft as a whole but have a direct impact on spacecraft FSS. Agrawal gives an overview of the spacecraft design process as a system., with specific chapters related to structural design, thermal control, and communication systems [6].

The primary structural requirements are that the FSS structure must survive launch loads and vibrations. The maximum limit load factors are 3–5 g's in axial and lateral loads, varying on configuration and launch vehicle. Each launch vehicle has a specific launch load profile. This affects the FSS because the load requirement is met by adding sufficient structural mass to the dielectric structure or support structures to provide required mechanical properties. The added mass directly relates to additional losses in the FSS performance and is incorporated into the design and loss budget. Another mechanical requirement is that all honeycomb core structures must be vented to allow for launch depressurization. The dimensional stability requirement to maintain grid tolerance also has to be maintained and incorporated into the design.

Environmental and contamination requirements result from the local environment and proximity of the FSS to sensitive optics. The most basic environmental concerns result from the temperature and vacuum environment of space. The goal of the thermal control is to minimize temperature variations to maintain good RF performance. As mentioned, this is usually achieved by the application of a thermal control paint or coating. The space vacuum environment makes electrostatic discharge a concern. Since FSSs are made of dielectric materials, this is a problem in FSS design. This requirement is met by careful design of the grid elements to dissipate charge buildup or by having a slightly conductive thermal control paint. The requirement is usually stated as a minimum surface resistivity to be achieved. The materials

must be able to survive in the radiation environment of space, since radiation can degrade the electrical and mechanical properties of the FSS and supporting structures. Scientific instruments on spacecraft often have special additional requirements. If there are optics within the proximity of the FSS, there may be specific contamination requirements for material outgassing. A magnetometer scientific would also levy magnetic requirements within its field of view. This is just a brief list of environmental requirements that are general to most spacecraft. The specific mission and operation of the individual spacecraft will have direct requirements that must be incorporated into the design and fabrication of spacecraft FSSs.

## REFERENCES


1. R. Jones, *Mechanics of Composite Materials*. Hemisphere, New York, 1975.
2. S. Tsai, *Composite Design*, 4th ed. Think Composites, Dayton, OH, 1988.
3. M. S. Schwartz, *Composite Materials Handbook*, 2nd ed. McGraw-Hill, New York, 1982.
4. C. Chamis, Simplified composite micromechanic equations for hygral, thermal, and mechanical properties. *SAMPE Q.*, April, pp. 14–23 (1984).
5. G. Hickey, Effect of electron radiation on polymer matrix systems. *Thermochim. Acta* 192, 199–208 (1991).
6. B. Agrawal, *Design of Geosynchronous Spacecraft*. Prentice-Hall, Englewood Cliffs, NJ, 1986.


*CHAPTER SEVEN*

# Active Beam Control Arrays

**LANCE B. SJOGREN**, RF Products Center, TRW Electronic Systems and Technology Division, Redondo Beach, California

With electronic devices embedded into their periodic cells, frequency selective surfaces (FSS) are capable of a broader range of functions. The earliest proposal for an array of this type appears to be that of Lee and Fong [1], involving the periodic loading of a corrugated surface with negative-resistance devices. It was envisioned that such an array would have the capability to amplify or shape a beam.

Aided by recent advances in the technology for high-frequency integrated circuits, such active FSS are now a reality. One simple form of active array consists of a metalization grid periodically loaded with biased linear diodes. Such an array is capable of modifying the amplitude or phase of a quasi-optical beam under external control. Since conventional high-frequency circuits that perform such functions are known as *control circuits*, this type of array has been given the name *beam control array*.

## 7.1 BACKGROUND

### 7.1.1 The Series-Resonant Beam Control Array

Beam control arrays developed up to now have been based on the series-resonant "self-resonant" grid [2, 3]. This FSS consists of an array of strips interrupted by gaps at periodic intervals (Figure 7.1a). In simple terms, this grid appears to a quasi-optical beam as an inductance (due to the strip array) in series with a capacitance (due to the gaps) (Figure 7.1(b)). In an active

*Frequency Selective Surface and Grid Array*, Edited by T. K. Wu
ISBN 0-471-31189-8 © 1995 John Wiley & Sons, Inc.